



Viscoelastic simulations using the closed-form Adaptive Length Scale (ALS-C) model

Konstantinos Zografos^{a,c,*}, Alexandre M. Afonso^b, Robert J. Poole^c

^a James Weir Fluids Laboratory, Department of Mechanical and Aerospace Engineering, University of Strathclyde, Glasgow G1 1XJ, UK

^b CEFT, Dep. Eng. Mecânica, Faculdade da Engenharia da Universidade do Porto, 4200-465 Porto, Portugal

^c School of Engineering, University of Liverpool, Brownlow Street, Liverpool L69 3GH, UK

ARTICLE INFO

Keywords:

Adaptive Length Scale
Viscoelastic fluids
Elongational flows
Shear flows
Contraction flows

ABSTRACT

In this paper we employ the closed-form of the Adaptive Length Scale Model (ALS-C) [Ghosh et al., “A new model for dilute polymer solutions in flows with strong extensional components”, *J. Rheol.* **46**, 1057–1089 (2002)] and we investigate its characteristics and potential to more accurately capture pressure-drop in contraction flows of viscoelastic fluids. The ALS-C model was originally derived based on purely homogeneous elongational flows in order to model coil-stretch hysteresis. However, in its originally proposed form we reveal a number of numerical issues which have not been analysed previously and are reported here considering both standard rheological flows, simple channel flows and complex flows within a 4:1 contraction. We demonstrate a new approach for evaluating the instantaneous change in the adaptive length scale as a result of instantaneous changes in the flow field, overcoming the need to employ other root-finding approaches. Guidelines are provided for the correct use of the employed local Weissenberg number and a modified approach is considered for the evolution equation of the actual extensibility, allowing its efficient use in complex numerical simulations. We illustrate that a suitable combination of the model parameters can produce behaviours that are found experimentally in viscoelastic fluids and we find that pressure-drop enhancements in flows within 4:1 contractions observed experimentally are achievable.

1. Introduction

Viscoelastic fluid flows within contractions and or contraction /expansions geometries (both planar and axisymmetric) have been, and continue to be, of great importance both from numerical and experimental perspectives. Flows of non-Newtonian fluids within these configurations manifest significantly different responses from the equivalent Newtonian fluid flows [1] as is illustrated in a variety of experimental [2–12] and numerical [13–18] studies. These different behaviours include the formation of vortices at the entrance region (both salient and entrance corners), the enhancement of the pressure-drop across the contraction and the generation of velocity overshoots along the flow centreline.

The experimental study of Binding and Walters [5] illustrated that pressure-drop enhancements can be observed for flows of Boger fluids both in axisymmetric and planar contraction geometries. In Fig. 1, reproduced from their study, it can be seen that at low flow rates Boger and Newtonian fluids demonstrate the same entry pressures. As the flow rates are increased the entry pressure of the former increases

significantly for both geometries, while as discussed in their study, the kinematics are not the same within the two geometries and significant differences exist. On the contrary, in a later study by Nigen and Walters [19] the flow of Boger fluids within axisymmetric contractions illustrated significant enhancements in the excess pressure-drop, while in the equivalent flows within planar contractions no clear differences were found in the evaluated pressure-drops between Boger and Newtonian fluids. The authors stated that differences between the fluid flows within planar configurations could only be observed through the kinematics when the flows were at high flow rates for the Boger fluids. These different findings highlight that rheological differences between Boger fluids are an important factor [20] and need to be carefully considered.

In addition, contraction flows have been chosen as “benchmark” problems for viscoelastic fluid flow modelling from a numerical perspective [21]. Coates et al. [22] examined the flow within both 4:1 and a 8:1 axisymmetric, abrupt, contractions using a modified version of the upper convected Maxwell model, in an attempt to reproduce

* Corresponding author at: James Weir Fluids Laboratory, Department of Mechanical and Aerospace Engineering, University of Strathclyde, Glasgow G1 1XJ, UK.

E-mail address: k.zografos@strath.ac.uk (K. Zografos).

<https://doi.org/10.1016/j.jnnfm.2022.104776>

Received 26 October 2021; Received in revised form 23 February 2022; Accepted 25 February 2022

Available online 8 March 2022

0377-0257/© 2022 The Authors. Published by Elsevier B.V. This is an open access article under the CC BY license (<http://creativecommons.org/licenses/by/4.0/>).

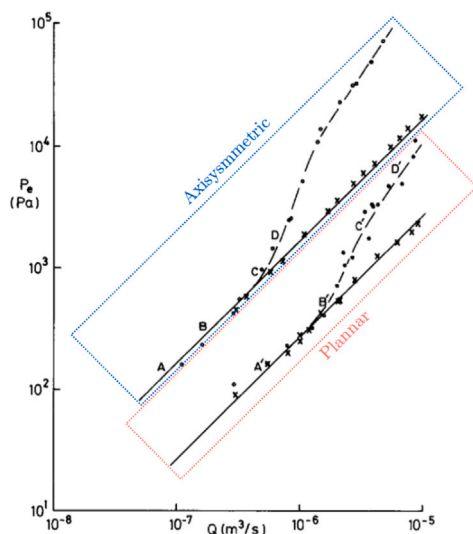


Fig. 1. Entry pressure data for the Boger fluid flow within axisymmetric and planar contraction geometries. Circular symbols are for the Boger fluids and cross symbols for Newtonian fluids. Reprinted from D. M. Binding and K. Walters, On the use of flow through a contraction in estimating the extensional viscosity of mobile polymer solutions, 30, 233–250 (1988) [5], with permission from Elsevier.

what it was observed experimentally by McKinley et al. [6] when investigating the flow of Boger fluids through such geometries. The authors illustrated that numerical simulations could produce a qualitative agreement in terms of the corner vortex formation, but they fail to predict the strong enhancement in pressure drop observed experimentally. In the numerical study of Aboubacar et al. [13], the authors investigated the flow of polymer solutions within planar and axisymmetric 4:1 contractions designed with and without rounded corners. They employed the Oldroyd-B model in order to investigate constant viscosity viscoelastic fluids, while they considered the linear and exponential forms of the Phan-Thien and Tanner (PTT) model to examine the influence of shear-thinning. Later, Alves et al. [14] reported benchmark solutions for the Oldroyd-B model and two forms of the PTT model (i.e. linear and exponential) within planar 4:1 contractions. Their study was in agreement with the results reported in Aboubacar et al. [13], with all viscoelastic models being unable to predict the large enhancements in pressure drop seen experimentally. Similar findings have also been reported in the study of Binding et al. [15], where the authors investigated pressure-drop related issues when employing the Oldroyd-B model within axisymmetric and planar 4:1 contractions, 1:4 expansions and 4:1:4 contraction/expansions. They focused on the effects of the solvent-to-total viscosity ratio and illustrated that pressure-drop enhancements could not be found, with the highly concentrated polymer solutions exhibiting smaller values of pressure-drop and deviating more from the Newtonian response.

The above numerical studies demonstrated that currently the most commonly employed closed-form viscoelastic models are able to predict qualitatively the formation of upstream vortices in contractions (or contraction/expansions) and report the onset of elastic instabilities that occur for further increases of the characteristic Weissenberg number. Their failure [1] however to provide accurate estimates for the pressure-drop, which is today a well-known problem of the closed form constitutive models, is important and, as was stated in Rothstein and McKinley [8], the constitutive models should be able to predict the large pressure-drop enhancements observed experimentally in stable laminar flows.

The use of contraction or contraction/expansion configurations, is not limited to studies that focus solely on the investigation of the rich dynamics of viscoelastic fluids. Designs of this type or equivalent that generate similar dynamics are encountered in a range of engineering

applications and thus, providing meaningful pressure drop measurements is of practical importance. Geometries with a contraction or contraction/expansion have been identified as appropriate platforms for performing measurements and studies related to the extensional rheology of viscoelastic fluids [23–31] and for characterising other samples of interest, such as DNA, or blood plasma [32–34], red blood cells [35,36] and capsules [37,38]. Furthermore, being able to evaluate accurately the pressure-drop will be beneficial for the design of microfluidic chips such as those being used as rectifiers, or for those used as platforms for replicating flows within porous media [39–43].

Constitutive equations that are derived from elastic dumbbell models are very popular for use in numerical simulations. They are commonly quite inexpensive [44,45] but they also introduce concepts that are related to the underlying physics, thus offering a connection between macroscopic elements and microstructure [44]. The Finite Extensible Non-Linear Elastic (FENE) representation of a polymer molecule is very popular, since it provides realistic behaviour [46] and various closures have been proposed for deriving models from the kinetic theory for use in analytical or computational analysis. Applying closures to the models from kinetic theory however, impacts significantly the rheological responses [47]. The most popular closure used in computational fluid dynamics (CFD) simulations is provided by the FENE-P model [48], where P stands for the Peterlin approximation but this closure is known to be problematic. Other closures have also been proposed [49] in attempt to fix the poor approximation of the FENE kinetic theory that were induced by the Peterlin approximation, especially for transient flows. Lielens et al. [49] have proposed the FENE-L and FENE-LS closures and used their models in stochastic simulations to illustrate better approximations to the responses predicted by the FENE representation for several rheometrical flows. Chilcott and Ralison [50] proposed the FENE-CR model, a modification of the FENE-P model, which would be more appropriate to describe Boger fluids. Their model was able to keep the basic characteristics of the FENE-P and predict a constant shear viscosity instead of shear-thinning that the FENE-P model predicts. Further extensions of the FENE-CR have also been proposed, such as the FENE-MCR model [22] and the FENE-CD [44].

Recent advances in numerical simulations and procedures have indicated some progress regarding the pressure-drop issue. Koppol et al. [51] used a multi-scale simulation approach and investigated numerically the flow within a 4:1:4 contraction/expansion and compared their findings with the experimental study of Rothstein and McKinley [8]. The authors illustrated the ability to capture a pressure-drop enhancement for all the cases examined, however the extensibility parameter values employed were far lower from those reported in Rothstein and McKinley [8]. In the study of Nystrom et al. [52], the authors simulated viscoelastic fluid flows within several types of axisymmetric 4:1 contractions using the FENE-CR model to reflect the flow of a Boger fluid. The authors demonstrated for three different, but relatively small (and unlikely physical), values of the extensibility parameter that the model manages to predict some enhancement in the pressure drop for dilute polymer solutions, despite the fact that the model possesses weaker first normal-stresses compared to the Oldroyd-B model. In Zografos et al. [30], the authors investigated numerically the flow of viscoelastic fluids within a smooth hyperbolic contraction/expansion geometry and demonstrated that some small enhancements in pressure-drop can be obtained when using the FENE-P model. Further advances on the issue have been reported in Jahromi et al. [53]. The authors proposed a hybrid model which combines the White–Metzner and FENE-CR models and illustrated that the model could capture the pressure-drop enhancements observed in Rothstein and McKinley [8]. Their “swanINNF” model uses a dissipative function which employs the actual extensional strain rate evaluated by the flow invariants. The function was proposed to have two different versions (swanINNF(c) and swanINNF(q)) resulting in different responses when controlling a material dissipative extensional-viscous time-scale that was introduced

as an internal parameter. However, both versions of the model predict an unbounded extensional viscosity in steady extensional flow. The work was extended further in López-Aguilar et al. [54,55], where a multimodal version of the swanINNF(q) version (swIM) was proposed together with the swanINNF(q)+ development (swAM), demonstrating the capabilities of the model when investigating the flow of dilute polymer solutions in a range of different geometries and in particular showing good agreement with the experimental findings of Nigen and Walters [19]. The efficiency of the model was later demonstrated in Webster et al. [20], where the authors managed to reproduce what was found in the experimental study of Binding and Walters [5] in terms of pressure-drop. It should be mentioned however that despite these advances, for all the above studies the values of the employed extensibility parameters were relatively small in contrast to what has been typically reported for experimental fluids [8,56] and the models are basically empirical.

Despite these advances in numerical modelling, there is still plenty of room left for new simple closed-form models that will bridge the gap with experiments. In this study we employ the closed form of the adaptive length scale model (ALS-C) proposed by Ghosh et al. [45] and illustrate its performance when it is used in CFD. As we discuss in the following sections, the model (both in the stochastic and closed form) follows the FENE representation. In the original paper it was shown that although a single FENE chain is very efficient when evaluating the behaviour of a polymer at large strains, on the contrary it is inadequate for capturing the correct behaviour in slowly deforming regions for which multiple chains are required in order to capture more accurately the occurring physics. Since this is computationally very expensive, the basic idea that led to the derivation of the adaptive length scale model and its closed-form is the requirement for a model that can approximate these polymer dynamics using a single spring. To our knowledge this is the first time the ALS-C model is used in CFD simulations and we report its behaviour for a simple straight 2D channel flow and investigate the benchmark problem of a 2D, planar, 4:1 contraction.

The rest of the paper is organised as follows: In Section 2 the basic equations describing the ALS-C model are presented and the modifications considered are discussed. In Section 3 the rheometric properties of the model are demonstrated considering the case of a steady-state planar extensional flow and the case of a steady-state shear flow. Then in Section 4 the performance of the model in CFD simulations is illustrated for different values of its internal parameters, while comparisons with the responses of the FENE-P model are provided. Finally, in Section 5 conclusions are given together with an outlook for further work.

2. Governing equations

The basic equations describing the flow of a viscoelastic fluid modelled by the ALS-C model are firstly presented. The derivation together with an in-depth analysis of the origins of these equations and their correlation with principles from kinetic theory have been extensively discussed in Ghosh et al. [45] and Gupta [57] and thus, we do not unnecessarily repeat them here but simply refer interested readers to these original papers. The adaptive length scale model proposed by Ghosh et al. [45] introduces new physical variables that are based on an important concept. Assuming a generic quantity ϕ , the concept suggests that specific quantities able to capture the instantaneous changes to molecular parameters in the limit of instantaneous changes of the flow field should be considered, and are denoted with an asterisk, ϕ^* . However, the drawback of this approach is that the effects of these instantaneous changes and the use of ϕ^* directly in any constitutive equation for the polymeric stress may lead to instantaneous “jumps” in the polymeric stress contributions. As Ghosh et al. [45] argued, such jumps are unphysical and are not observed experimentally, and therefore new equivalent quantities should be introduced for which the asterisks are dropped to distinguish from that limit

i.e. ϕ . These new variables describe the behaviour of microstructural information without the instantaneous change assumption, and have the tendency to go towards the pseudo steady-state that is described by ϕ^* (i.e. instantaneous molecular change limit).

Before presenting our analysis, we slightly modify the notation used in Ghosh et al. [45], in order to aid the readability of the equations and make, in our view, the forthcoming analysis more easy to follow. The ALS-C model does not consider the behaviour of each individual polymer molecule (as the stochastic version does), but rather employs average values of the required quantities (e.g. $\langle\phi\rangle$ and $\langle\phi^*\rangle$). As such, the average and instantaneous adaptive length scale is defined as $\langle b_{\text{seg}}^*\rangle$ and is related to the polymer molecule extensibility which adjusts to the local flow. In our analysis here we will only consider the closed form of the adaptive length scale model, thus henceforth the brackets which indicate average values are dropped and we simply define $\langle b_{\text{seg}}^*\rangle \equiv b_s^*$. As explained previously, although the idea of instantaneous jumps is essential in order to capture sudden flow changes, this would result in unphysical jumps in the polymer contribution to the stresses. Thus, the “real” adaptive length scale is defined as $\langle b_{\text{seg}}\rangle \equiv b_s$, which approaches the pseudo steady-state of the instantaneous extensibility parameter b_s^* . When the maximum extension is reached both dimensionless extensibility parameters obtain the maximum molecular extension b_m (defined as b_{max} in Ghosh et al. [45]). Finally, we will compare our ALS-C results extensively with the FENE-P model [48]. We note that $b_m \equiv L^2$ or $b_m \equiv L^2 - 3$ depending on the version of the FENE-P considered, where L^2 is the usual notation employed for the maximum extensibility parameter of the FENE-P model [58].

2.1. The closed form adaptive length scale (ALS-C) model

The closed-form equation for evaluating the instantaneous adaptive length scale based on our notation is expressed as follows

$$\frac{\text{Wi}^{\text{eff}}}{K^*} \left(1 - \frac{\text{Tr} \mathbf{A}}{b_s^*} \frac{b_m}{b_s^*} \right) = z, \quad (1)$$

where $\text{Tr} \mathbf{A}$ is the trace of the conformation tensor \mathbf{A} , while z is an “order one” model constant that controls the behaviour of b_s^* . According to Ghosh et al. [45], the precise value cannot be set by the theory, but when $z < 1$ rapid growth of stresses is expected. The effects of varying z are examined in Section 3.2. Ghosh et al. [45] proposed that the evolution equation to be developed for the polymer extensibility (discussed in Section 2.2) should include a stiffening term that will cause b_s to decrease towards b_s^* . The required stiffening was suggested to be proportional to the effective Weissenberg number, Wi^{eff} , appearing in the left hand side of Eq. (1) and is defined as

$$\text{Wi}^{\text{eff}} = \frac{1}{2} \lambda \text{Eig}(\dot{\gamma}^{\text{eff}}), \quad (2)$$

where λ is the relaxation time, and $\text{Eig}(\dot{\gamma}^{\text{eff}})$ is the maximum eigenvalue of an effective rate-of-strain tensor elegantly defined as:

$$\dot{\gamma}^{\text{eff}} = \begin{bmatrix} \dot{\gamma}_{11} & s\dot{\gamma}_{12} & s\dot{\gamma}_{13} \\ s\dot{\gamma}_{21} & \dot{\gamma}_{22} & s\dot{\gamma}_{23} \\ s\dot{\gamma}_{31} & s\dot{\gamma}_{32} & \dot{\gamma}_{33} \end{bmatrix}, \quad (3)$$

where $s = (b_0/b_m)^{1/2}$ is a parameter that multiplies the off-diagonal elements of the shear-rate tensor (when $s = 1$, $\dot{\gamma}^{\text{eff}} \equiv \dot{\gamma} = [\nabla \mathbf{u} + (\nabla \mathbf{u})^T]$, where \mathbf{u} is the velocity vector) and b_0 is an appropriate fitting parameter that controls the onset of the shear-thinning behaviour Ghosh et al. [45]. In the following sections we investigate and report the influence of both the z and s parameters.

Ghosh et al. [45] restricted their analysis to homogeneous shear or extensional flow and used in Eq. (1) the characteristic Weissenberg number for each specific case. In contrast we employ Wi^{eff} throughout, since it is a more appropriate choice when dealing with general flows where the local deformation is changing and is not constant as in the homogeneous viscometric flows dealt with in Ghosh et al. [45]. Finally,

the parameter K^* appearing in Eq. (1) is a dimensionless parameter defined as [45,57]:

$$K^* = \frac{b_s^*}{b_s^* + 5} \left(\frac{\sqrt{(b_m + 5)(b_m + 7)}}{b_m} \right) \times \left(\frac{[2(M^* + 1)^2 + 7][(M^* + 1)^2 - 1]}{45} - \frac{12[(M^* + 1)^2 + 1][(M^* + 1)^2 - 1]^{1/2}}{45(M^* + 1)(b_s^* + 7)} \right), \quad (4)$$

where, $M^* = b_m/b_s^*$, is the number of segments or equal-length springs that represent the polymer chain. From its definition it is obvious that since $b_s^* \leq b_m$ then $M^* \geq 1$.

The solution of Eq. (1) for a given flow field (i.e. known Wi^{eff} , TrA) and desired fluid properties (b_m , z , s), will provide the appropriate values for the adaptive length scale. In order to obtain this solution exactly a root finding method is required, such as a standard bisection method that was employed in Burmenko [59]. Employing the ALS-C model in finite volumes or other standard computational fluid dynamics (CFD) simulations, Eq. (1) will have to be solved at every computational cell that is discretising the physical domain. Using a root finding method is expected to add extra computational costs and for that reason a different approach is followed here which is more computationally efficient. More details on how M^* is approximated are given in Section 2.4.

2.2. Evolution equation of the polymer extensibility

Once the value of the adaptive length scale is approximated, then the dimensionless evolution of the polymer's extensibility b_s can be evaluated using the following formula:

$$\frac{db_s}{d\hat{t}} = -|\mathbf{n}_\gamma \times \mathbf{n}_A| Wi^{eff} \left(1 - \frac{TrA b_m}{(b_s^*)^2} \right) (b_s - b_s^*) K^* + (b_m - b_s) K, \quad (5)$$

where, $\hat{t} = t/\lambda$, is the dimensionless time, K is a dimensionless parameter evaluated in an identical manner as K^* using Eq. (4) and by dropping all stars ($b_s^* \equiv b_s$ and $M^* \equiv M = b_m/b_s$). The unit vectors \mathbf{n}_γ and \mathbf{n}_A are each parallel to the eigenvectors that correspond to the largest eigenvalues of the rate-of-strain tensor and the conformation tensor respectively. The first term of the right-hand side of Eq. (5) is a stiffening term which causes b_s to decrease towards b_s^* , while the second term acts as a relaxation term which makes the adaptive length scale to return to b_m [45,57]. In Ghosh et al. [45], the authors considered a different approach and instead of \mathbf{n}_A , a vector that is composed by the square root of the diagonal elements of \mathbf{A} normalised by $(TrA)^{1/2}$ was used (see Eq. (52) in Ghosh et al. [45]). This approach was considered valid for a Protean coordinate system [60–62], which the authors employed in their analysis. The coordinates of a system of this type are provided by the streamlines and the lines orthogonal to them. However, such a Protean system is limited to 2D flows and flows that are without recirculation regions and thus, it has a very limited usage especially for investigating general flows [1]. As a consequence we use Eq. (5) throughout. In Appendix A a discussion is provided demonstrating the important issues met when the original approach is considered.

Fig. 2 demonstrates the non-monotonic expected behaviours of the instantaneous (b_s^*) and actual (b_s) extensibilities, in contrast with the constant value of the FENE-P extensibility parameter (L^2) for a steady homogeneous pure shear flow with increasing Wi , defined as $Wi = \lambda \dot{\gamma}_0$. It can be seen that at low Weissenberg numbers the behaviour of b_s^* and b_s is identical and equal to L^2 . At moderate Wi , both the instantaneous and actual extensibilities start to deviate from b_m . The former decreases to a minimum value, while the latter demonstrates a similar trend but with a higher minimum value. At higher Wi , they both start to increase until they asymptotically return to the value of $b_m \equiv L^2$ in the limit $Wi \rightarrow \infty$. Finally, as can be seen by the model equations, Eqs. (1), (2), (4) and (5), b_s and b_s^* do not depend upon the polymer concentration of the fluid (i.e. representing a dilute polymer solution or otherwise). This behaviour is independent of the solvent-to-total viscosity ratio $\beta = \eta_s/\eta_0$, where η_s is the solvent viscosity, $\eta_0 = \eta_s + \eta_p$ is the total zero-shear viscosity and η_p the polymer viscosity.

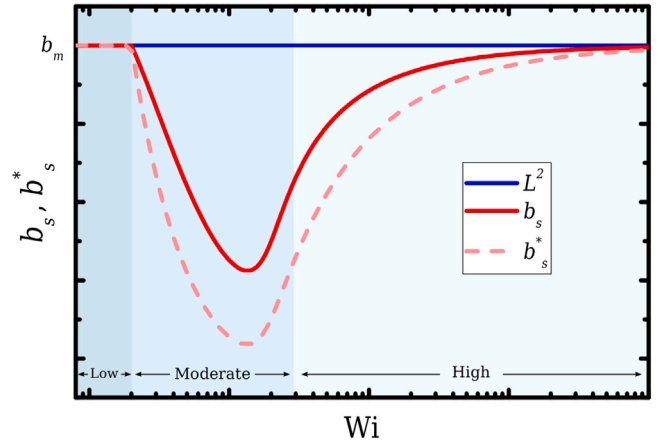


Fig. 2. Qualitative behaviour of the real (b_s) and the instantaneous (b_s^*) extensibilities of the ALS-C model, in comparison with the FENE-P extensibility parameter (L^2) for increasing values of Weissenberg numbers when in homogeneous steady shear flows.

2.3. Evolution equation of the conformation tensor

The evolution equation of the conformation tensor for the ALS-C model follows the Peterlin approximation, similar to the FENE-P model [48], and is written in dimensionless form as:

$$\frac{d\mathbf{A}}{d\hat{t}} = Wi [\nabla \mathbf{u}^T \cdot \mathbf{A} + \mathbf{A} \cdot \nabla \mathbf{u}] - \frac{K\mathbf{A}}{\left(1 - \frac{TrA}{b_s} \frac{b_m}{b_s}\right)} + K \left(\frac{b_s}{b_m} \right) \mathbf{I}, \quad (6)$$

where \mathbf{I} is the identity tensor. It worth noting that Eq. (6) proposed in Ghosh et al. [45] does not include the convection term of the conformation tensor, since the authors consider homogeneous flows. Since we are interested in general flows and in order to make use of the complete upper convected derivative we take into account the missing $\mathbf{u} \cdot \nabla \mathbf{A}$ term. Eq. (6) can therefore be expressed as

$$\overset{\nabla}{\lambda} \mathbf{A} = - \frac{K\mathbf{A}}{\left(1 - \frac{TrA}{b_s} \frac{b_m}{b_s}\right)} + K \left(\frac{b_s}{b_m} \right) \mathbf{I}, \quad (7)$$

where $\overset{\nabla}{\lambda} \mathbf{A} = (\partial \mathbf{A} / \partial \hat{t}) + \mathbf{u} \cdot \nabla \mathbf{A} - [\nabla \mathbf{u}^T \cdot \mathbf{A} + \mathbf{A} \cdot \nabla \mathbf{u}]$ is the upper convected derivative of the conformation tensor [63].

The polymeric contributions to the stress tensor for the ALS-C model are evaluated from the conformation tensor [45]:

$$\boldsymbol{\tau}_p = \frac{\eta_p}{\lambda} \left[\left(\frac{b_m}{b_s} \right)^2 \frac{\mathbf{A}}{1 - \frac{TrA}{b_s} \frac{b_m}{b_s}} - \frac{b_m}{b_s} \mathbf{I} \right]. \quad (8)$$

At this point it is worth comparing directly the above expression for the ALS-C model with the equivalent for the widely used FENE-P model [48]. The correlation between the stress tensor and the conformation tensor for the FENE-P model is written in Kramers' form [30, 64,65]:

$$\boldsymbol{\tau}_p = \frac{\eta_p}{\lambda} \left(f_A \mathbf{A} - a \mathbf{I} \right), \quad (9)$$

where $f_A = L^2 / (L^2 - TrA)$ is a function of the trace of the conformation tensor and a is a function of L^2 , $a = L^2 / (L^2 - 3)$. Comparing Eqs. (8) and (9) it can be seen that when the Weissenberg number is very low or very large, for which $b_s \simeq b_m$ (see Fig. 2), the stress tensor of the ALS-C model becomes

$$\boldsymbol{\tau}_p = \frac{\eta_p}{\lambda} \left[\frac{\mathbf{A}}{1 - \frac{TrA}{b_m}} - \mathbf{I} \right], \quad (10)$$

which is very similar with the FENE-P model ($b_m \equiv L^2$), except for the term multiplied by the identity tensor. On the contrary, at moderate

Weissenberg numbers it can be seen that Eq. (8), becomes:

$$\tau_p = M \frac{\eta_p}{\lambda} \left[\frac{MA}{1 - \frac{M^2 \text{Tr}A}{b_m}} - \mathbf{I} \right]. \quad (11)$$

Practically, this shows that all the important contributions are multiplied by the number of segments M , which is larger than unity ($b_s < b_m$).

2.4. Numerical implementation

The numerical procedure employing the equations of the ALS-C model is implemented within our in-house finite volume, CFD solver, which follows the discretisation principles described in Oliveira et al. [66], Alves et al. [14] and Afonso et al. [67]. The cases we are investigating here consider incompressible and isothermal fluid flows. Therefore, the continuity and the momentum equations are employed and solved numerically:

$$\nabla \cdot \mathbf{u} = 0, \quad (12)$$

$$\rho \left(\frac{\partial \mathbf{u}}{\partial t} + \mathbf{u} \cdot \nabla \mathbf{u} \right) = -\nabla p + \nabla \cdot \boldsymbol{\tau}, \quad (13)$$

where ρ is the fluid's density, p is the pressure and $\boldsymbol{\tau}$ is the extra stress tensor. The latter is expressed as the sum of the solvent stress component, $\boldsymbol{\tau}_s$ (Newtonian part), and the polymeric stress component:

$$\boldsymbol{\tau} = \boldsymbol{\tau}_s + \boldsymbol{\tau}_p = \eta_s \dot{\boldsymbol{\gamma}} + \boldsymbol{\tau}_p. \quad (14)$$

In this paper, we examine cases where the solvent-to-total-viscosity ratio is set as $\beta = 0.90$ and $\beta = 0.95$, a typical value for dilute polymer solutions, with Boger-fluid-like behaviour [7,8,68].

The evolution equation of the conformation tensor given in Eq. (16), is solved numerically within a finite-volume methodology, as described in detail in Afonso et al. [18,67], following the log-conformation approach [69] which employs the evolution of the logarithm of conformation tensor ($\Psi = \log A$). The evolution of the logarithm of the conformation is expressed in the form:

$$\frac{\partial \Psi}{\partial t} + \mathbf{u} \cdot \nabla \Psi - (\boldsymbol{\Omega} \Psi - \Psi \boldsymbol{\Omega}) - 2\mathbf{B} = -\frac{1}{\lambda} (f(e^\Psi) \mathbf{I} - f'[b] e^{-\Psi}), \quad (15)$$

where $\boldsymbol{\Omega}$ is a pure rotational component and \mathbf{B} a traceless extensional component. For further details and an in depth analysis the reader is referred to Fattal and Kupferman [69] and Afonso et al. [67]. The pressure and velocity fields are coupled using the SIMPLEC algorithm for collocated meshes by employing the Rhie and Chow interpolation technique [70]. The convective terms both in the momentum and the evolution equation of the logarithm of the conformation tensor, are discretised using the CUBISTA high-resolution scheme [14], while all diffusive terms are evaluated with central differences. All the calculations here were carried out at a vanishing Reynolds number, $\text{Re} \rightarrow 0$ (creeping flow conditions are imposed by ensuring the convective term, $\mathbf{u} \cdot \nabla \mathbf{u}$, in the momentum equation is identically zero, Eq. (13)), where we seek only steady-state solutions. Once the velocity, stress and conformation tensor fields are evaluated, Eq. (5) is solved to obtain the behaviour of b_s . The ordinary differential equation is solved explicitly subdividing the employed time step into a number of smaller internal steps (i.e. 10) for a more accurate evaluation of the time derivative.

Finally, the M^* parameter introduced in Section 2.1 is approximated by employing a quadratic function which describes its relationship with K^* . As can be seen in Fig. 3, the behaviour of K^* (Eq. (4)) as function of M^* for different values of maximum polymer extensibility can be approximated by a quadratic function, f_Q , fairly well over a large range of both M^* and b_m . Interestingly K^* appears to be insensitive to b_m , considering a range of b_m values that are typically used when studying numerically polymer molecules ($300 \leq b_m \leq 10000$) [7, 8,30,56,64,71]. Therefore, K^* is replaced here by $f_Q = a_1 M^2 + a_2 M + a_3$ and Eq. (1) is modified to read:

$$\frac{\text{Wi}^{\text{eff}}}{f_Q} \left(1 - \frac{\text{Tr}A}{b_m} (M^*)^2 \right) = z. \quad (16)$$

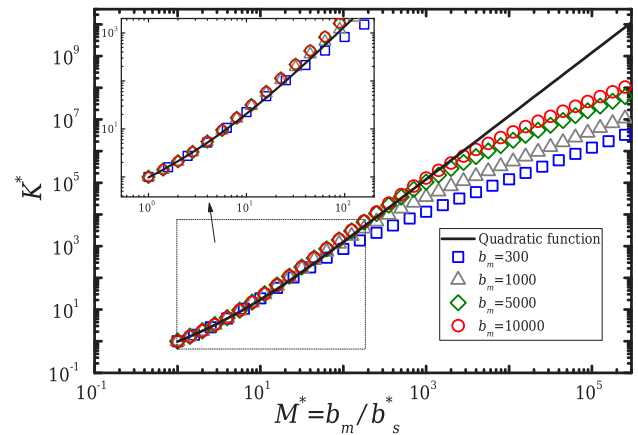


Fig. 3. Behaviour of K^* parameter as function of M^* for different values of b_m together with a quadratic fit function $f_Q = a_1 M^2 + a_2 M + a_3$, where $a_1 = 0.128$, $a_2 = 0.774$ and $a_3 = 0.0648$. The dashed box highlights the region where the majority of significant variations of M^* occur.

The coefficients of the quadratic function are taken to be $a_1 = 0.128$, $a_2 = 0.774$ and $a_3 = 0.0648$. After some mathematical rearrangements of Eq. (16), M^* is evaluated explicitly by using:

$$M^* = \frac{-a_2 z + \sqrt{a_2^2 z^2 - 4 \left(z a_1 + \text{Wi}^{\text{eff}} \frac{\text{Tr}A}{b_m} \right) (a_3 z - \text{Wi}^{\text{eff}})}}{2(z a_1 + \text{Wi}^{\text{eff}} \frac{\text{Tr}A}{b_m})}. \quad (17)$$

Once M^* is obtained, the instantaneous extensibility is known since $b_s^* = b_m / M^*$.

3. Rheometric properties

The predictions of the model with standard homogeneous viscometric flows are illustrated here. In particular the behaviour of steady-state planar extensional and steady-state shear flows is examined. The responses of the ALS-C model are always compared with the equivalent case of the FENE-P model.

3.1. Steady-state planar extensional flow

The case of a steady-state planar extensional flow is a category of the “shear-free” flows which are considered as one of the standard flows of rheology [72,73]. This type of extensional flow allows deformation only along two dimensions (2D) and is produced by a velocity field that is defined as $\mathbf{u} = (\dot{\epsilon}_0 x_1, -\dot{\epsilon}_0 x_2, 0)$. This field stretches the fluid element across the x_1 direction and squeezes it along the x_2 direction, where $\dot{\epsilon}_0$ is the constant applied strain-rate of the deformation and x_1, x_2 are the Cartesian coordinates. This velocity field will result in a shear-rate tensor that is given by:

$$\dot{\boldsymbol{\gamma}} = [\nabla \mathbf{u} + (\nabla \mathbf{u})^T] = \begin{bmatrix} 2\dot{\epsilon}_0 & 0 & 0 \\ 0 & -2\dot{\epsilon}_0 & 0 \\ 0 & 0 & 0 \end{bmatrix}. \quad (18)$$

Evaluating the eigenvalues of the shear-rate tensor ($\det(\theta \mathbf{I} - \dot{\boldsymbol{\gamma}}) = 0$), three real values exist, $\theta_1 = 2\dot{\epsilon}_0$, $\theta_2 = -2\dot{\epsilon}_0$ and $\theta_3 = 0$, for which the corresponding normalised eigenvectors are $\mathbf{n}_1 = (1, 0, 0)$, $\mathbf{n}_2 = (0, 1, 0)$ and $\mathbf{n}_3 = (0, 0, 1)$. In Section 2.2, Wi^{eff} was introduced as a function of the maximum eigenvalue and thus, from Eq. (2) $\text{Wi}^{\text{eff}} = \lambda \dot{\epsilon}_0$. Additionally, from Eq. (18) it can be seen that the s parameter is not influencing the response of the ALS-C model when in steady-state uniaxial planar flow (and any of the other equivalent types e.g. uniaxial or biaxial extension).

Solving numerically the equations for a planar extensional flow using MATLAB®, the response of the ALS-C model with $\beta = 0$ and

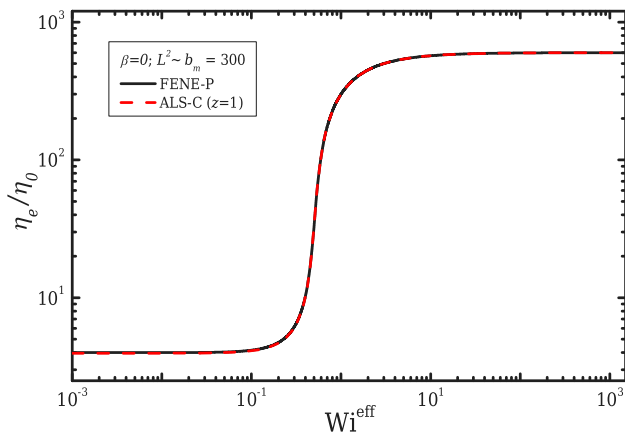


Fig. 4. Normalised planar extensibility of the ALS-C model for $\beta = 0$ ($\eta_s/\eta_0 = 0$) when $b_m = 300$ and $z = 1$ for increasing Wi in contrast with the equivalent behaviour of the FENE-P.

$b_m = 300$ when $z = 1$ is shown in Fig. 4 in contrast to the equivalent behaviour of the FENE-P model with $\beta = 0$ and $L^2 = 300$. For the ideal case of a steady-state planar extensional flow ($db_s/d\hat{t} = 0$), b_s^* is expected to obtain instantaneously the value of b_m [45], and thus, Eq. (5) results in $b_s = b_m$. Since no variations of the actual extensibility occur, the response of the model is equivalent to the FENE-P model, where both models illustrate that coil-stretch transition occurs around $Wi^{eff} \simeq 0.5$ [45] (we note we have checked the same behaviour occurs for the case of uniaxial extension, where the ALS-C and FENE-P responses models also match). Finally we note this response is the same for any other value of z , since the first term of the right-hand side of Eq. (5) will be zero and thus Eq. (1) is not influencing the result.

3.2. Steady-state shear flow

Steady-state shear flow is probably the most widely-studied viscometric flow [72,73]. As mentioned in Section 2.1, the formulation of the ALS-C proposed by Ghosh et al. [45] is based on a Protean coordinate system. As perhaps expected, we found that using this formulation in a general (non Protean) coordinate system gave results dependent on the frame of the problem and suffered from significant issues that need to be addressed in order to achieve stable solutions for CFD. In Appendix A, a discussion illustrating these issues when the original approach is considered is provided. The employed Eq. (5) on the other hand, does not suffer from these issues and so we refrain from a more detailed discussion here.

Considering the case of a Couette flow in which the top wall is moving and the bottom remains fixed, the velocity profile describing the flow in Cartesian coordinates is $\mathbf{u} = (\dot{\gamma}_0 x_2, 0, 0)$, where $\dot{\gamma}_0$ is the constant shear-rate experienced by a fluid element along the x_2 direction. The shear-rate tensor for this velocity field will have the form:

$$\dot{\boldsymbol{\gamma}} = [\nabla \mathbf{u} + (\nabla \mathbf{u})^T] = \begin{bmatrix} 0 & s\dot{\gamma}_0 & 0 \\ s\dot{\gamma}_0 & 0 & 0 \\ 0 & 0 & 0 \end{bmatrix}. \quad (19)$$

The three eigenvalues of the shear rate tensor will be $\theta_1 = s\dot{\gamma}_0$, $\theta_2 = -s\dot{\gamma}_0$ and $\theta_3 = 0$, with their three corresponding normalised eigenvectors being $\mathbf{n}_{\gamma,1} = (1/\sqrt{2}, 1/\sqrt{2}, 0)$, $\mathbf{n}_{\gamma,2} = (1/\sqrt{2}, -1/\sqrt{2}, 0)$ and $\mathbf{n}_{\gamma,3} = (0, 0, 1)$. Considering Eq. (2) the effective Weissenberg for this case is $Wi^{eff} = \lambda s \dot{\gamma}_0 / 2$ and thus we have $Wi = \lambda \dot{\gamma}_0 \equiv 2Wi^{eff}/s$. In order to plot all cases investigated in a consistent manner and maintain Wi as the characteristic Weissenberg number, we introduce a local Weissenberg number Wi^* defined as $Wi^* = 2Wi^{eff}/s$.

3.2.1. Influence of the z parameter on steady-state shear flow

Here we demonstrate the effects of the z parameter in Eq. (16) on the behaviour of the ALS-C model, when under constant shear-rate deformation. A range of different values within the range $0.25 \leq z \leq 100$ for the same $b_m = 300$ value are presented in Fig. 5. More specifically, Fig. 5(a) shows the behaviour of b_s for increasing Weissenberg number. As $z \rightarrow 0$, b_s starts to deviate from b_m at lower Wi . For all cases except for those with large z values, a non-monotonic behaviour is observed. It can be seen that the smaller the z value, the lower the minimum obtained value for the actual extensibility. As Wi increases, b_s is asymptotically approaching the maximum extension ($b_m = 300$ for this case). When the value of z is large enough ($z = 100$) the model predicts exactly the same response as the FENE-P model, for which b_s remains constant and equal to b_m for all applied Wi . At steady-state conditions and when $Wi^{eff} \rightarrow 0$, Eq. (5) shows that b_s will not deviate from b_m . When $Wi^{eff} \gg 0$ it can be shown from Eq. (17) that $M^* = 1$ and thus Eq. (5) will reduce to $b_s = b_m$. The behaviour of b_s will influence the response of the conformation tensor \mathbf{A} and this is shown in Fig. 5(b) in terms of the first diagonal element of the conformation tensor with increasing Wi . For this velocity field, A_{11} contains the major contributions to the polymer stretching, with x_1 indicating the flow direction. When $z \gg 1$, A_{11} behaves exactly as in the case of the FENE-P model, while for moderate and low z values, A_{11} deviates from the FENE-P behaviour, introducing a range of new responses. Furthermore, in Fig. 6 the shear-thinning behaviour predicted by the ALS-C model and the response of the normalised first normal-stress difference for different values of z is shown. The shear-thinning behaviour for different values z is not significantly affected and all cases demonstrate a similar response overall as can be seen in Fig. 6(a). Minor deviations appear around $Wi = 2Wi^{eff} \sim 10$. Similarly, the normalised first normal-stress difference in shear has a different behaviour in the region where b_s is varying ($1 \leq Wi \leq 10^3$), while for $z = 100$, as expected, the model behaves exactly as in the case of the FENE-P model.

3.2.2. Influence of the s parameter on steady-state shear flow

In this section we illustrate the influence of the s parameter when in steady-state shear and how the viscometric properties are modified. Starting with the behaviour of the actual extensibility, Fig. 7(a) highlights different values of s when $b_m = 300$ and $z = 1$ for increasing Wi . It can be seen that changes in s result in the opposite behaviour than what was observed when changing z , with b_s decreasing further as s increases. The same effect is also observed in the behaviour of A_{11} , illustrated in Fig. 7(b). An important feature we found is that the response of the ALS-C model may have more than one solution branch as it can be seen for the case of $s = 2$ in Figs. 7(a) and 7(b) (i.e. non-unique values at a fixed value of Wi). The second solution was found by considering as an initialisation for each set of b_s and A_{ij} those sets that were obtained at a previous Wi^{eff} . If no initialisation is considered, the solution branch indicated by the solid line is obtained, for which b_s is advancing towards b_m around $Wi^* \sim 30$. On the contrary, when an initialisation is used, b_s advances to b_m at $Wi^* \sim 50$. As will be demonstrated also in Section 4, the existence of more than one solution depends on the choice of s , z and b_m parameters, and is not influenced only by the choice of s . Probably this issue is a reflection on the closure of the stochastic differential equations of the original model. Reviewing Figure 14 in Ghosh et al. [45], in which the stochastic and closed forms of the model are compared in terms of the predicted behaviour of b_s , it can be seen that as Wi increases b_s has a non-monotonic behaviour for the stochastic version. On the other hand for the ALS-C, b_s has the same behaviour as the one reported here.

As it was seen in Fig. 6(a), in a similar way in Fig. 8(a) the effects of s upon the onset of the shear-thinning behaviour are not important, with all cases demonstrating a similar behaviour as the local Weissenberg number increases. In the inset of Fig. 8(a), where the viscosity behaviour is plotted as a function of Wi^{eff} , it can be seen that

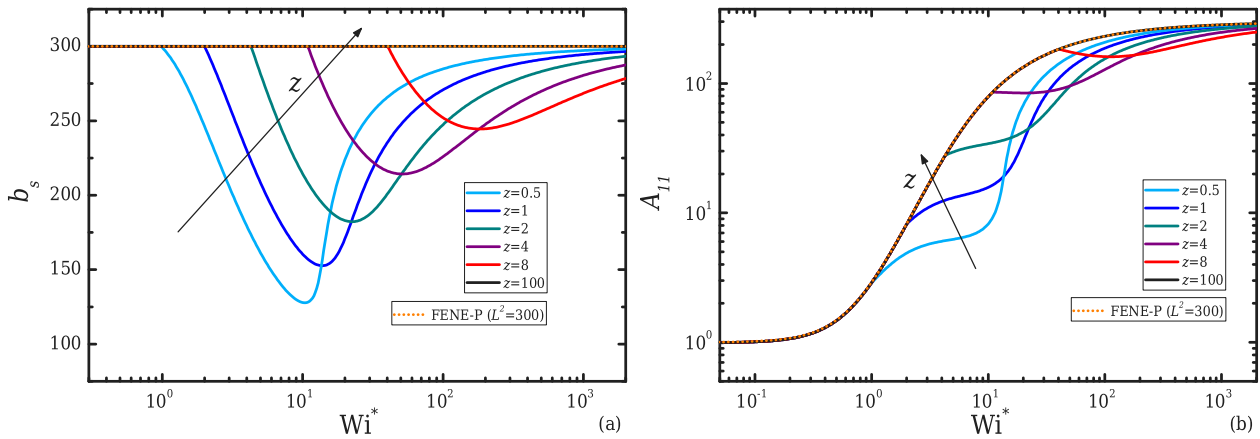


Fig. 5. Properties of the ALS-C model for different z values compared with the equivalent response of the FENE-P model, when $b_m = L^2 = 300$ and $s = 1$ for increasing $Wi^* = 2Wi^{eff}/s$: (a) Behaviour of b_s and (b) A_{11} element of the conformation tensor.

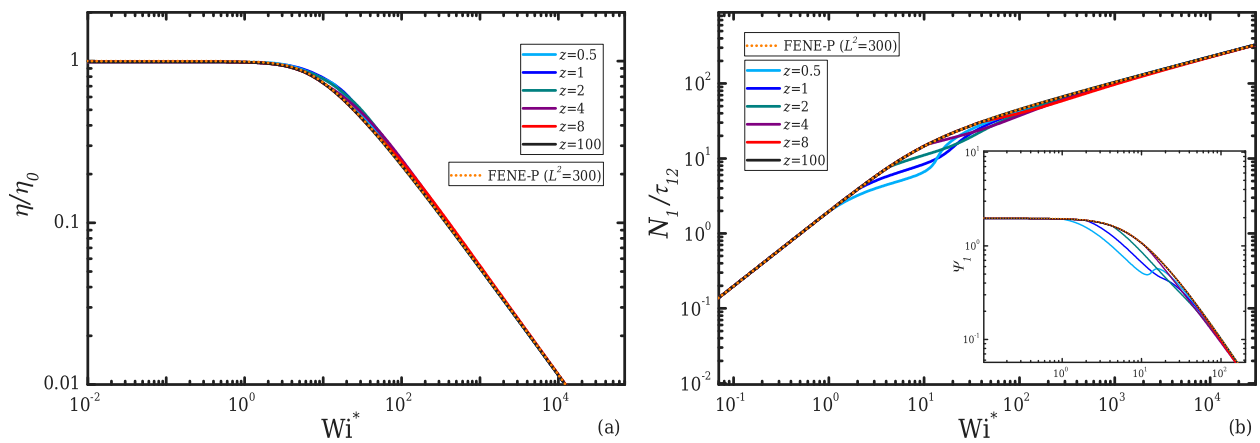


Fig. 6. Viscometric properties of the ALS-C model for different z values compared with the equivalent response of the FENE-P model, when $\beta = 0$ ($\eta_s/\eta_0 = 0$), $b_m = L^2 = 300$ and $s = 1$ for increasing $Wi^* = 2Wi^{eff}/s$: (a) Behaviour of the normalised shear viscosity and (b) normalised first normal-stress difference. The inset figure in (b) shows the behaviour of the first normal-stress coefficient Ψ_1 .

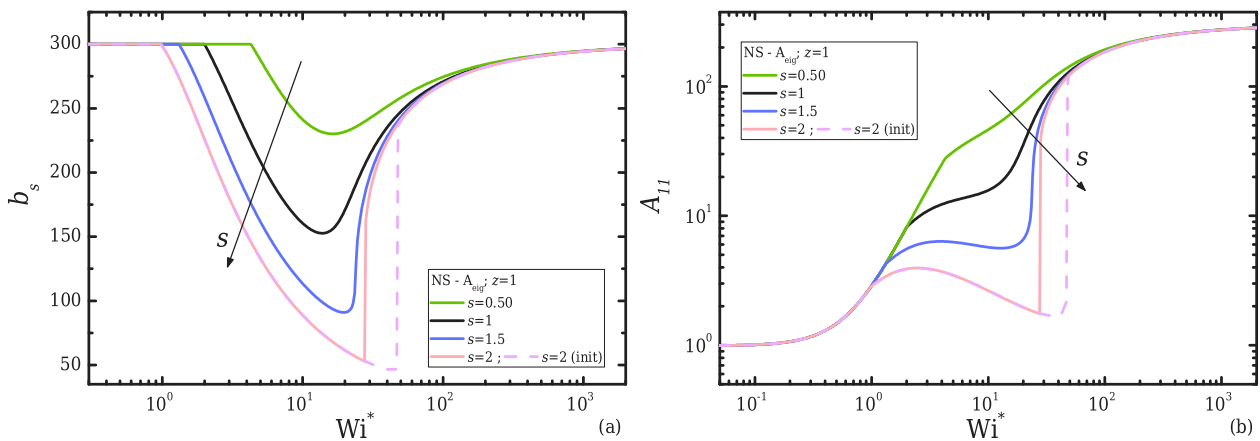


Fig. 7. Properties of the ALS-C model for different s values compared with the equivalent response of the FENE-P model, when $b_m = 300$ and $z = 1$ for increasing $Wi^* = 2Wi^{eff}/s$: (a) Behaviour of b_s and (b) A_{11} element of the conformation tensor.

now the onset of shear-thinning is controlled and starts earlier as s decreases. For $s = 2$ it can be seen that the shear viscosity produces some unphysical kinks. Similar responses have been also reported in the study of Inkson and Phillips [74] for the extended pom-pom model. For the ALS-C model, we found that this behaviour will always occur when the model is in regimes where more than one solution branch exist.

The inset figures of Figs. 6(b) and 8(b) illustrate the responses of the first normal stress coefficient for every case discussed. It is interesting to note that similar behaviours of Ψ_1 as those predicted for $z = 1$ and $z = 0.5$ (Fig. 6(b)) or the $s = 1$ and $s = 1.5$ cases (Fig. 8(b)), have been reported for real Boger fluids e.g. in the papers of McKinley et al. [6] and Rothstein and McKinley [6–8]. This type of behaviour is not possible to achieve with the FENE-P model and thus, the ALS-C

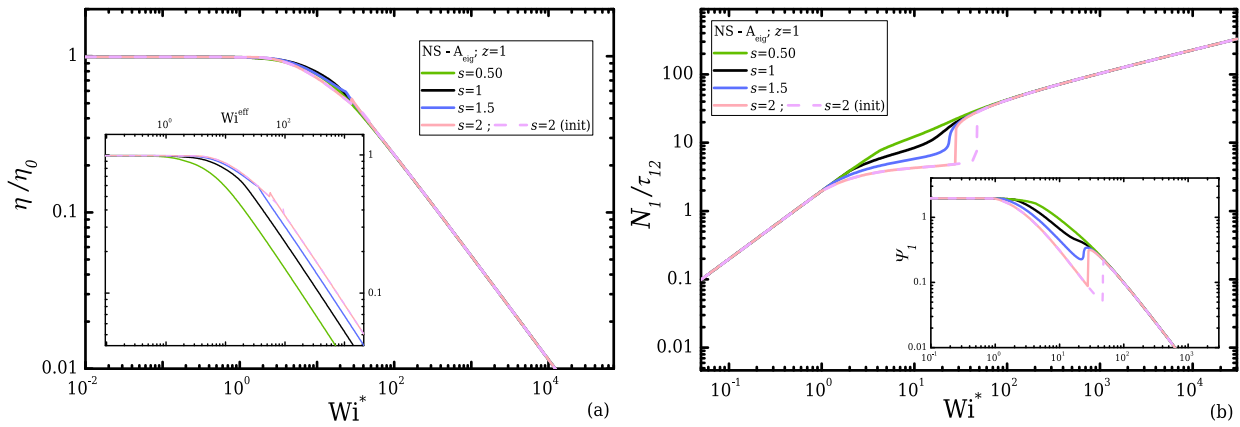


Fig. 8. Viscometric properties of the ALS-C model for different s , when $\beta = 0$ ($\eta_s/\eta_0 = 0$), $b_m = 300$ and $z = 1$ for increasing $Wi^* = 2Wi^{eff}/s$: (a) Behaviour of the normalised shear viscosity and (b) normalised first normal-stress difference. The inset figure in (b) shows the behaviour of the first normal-stress coefficient Ψ_1 .

model can provide a new range of behaviours that have been observed experimentally even in steady simple shear.

4. Results and discussion

In this section, the performance of the ALS-C model (Eqs. (5), (7) and (16)) and our numerical implementation will be presented. The accuracy of the numerical implementation is first validated by comparing the CFD results for the fully-developed case of a 2D channel flow against the viscometric properties of the steady-state shear flow. As fully-developed channel flow is viscometric these should be identical [75]. Following this benchmarking, the behaviour of the ALS-C model is extensively investigated in a more complex flow scenario of the flow in a 4:1 abrupt, planar, contraction for a range of different parameters.

4.1. Fully-developed channel flow (non-homogeneous steady shear)

In this section the performance of the CFD implementation employing the ALS-C model is discussed by investigating channel flow. For simplicity the analysis is for a 2D case, which corresponds to a planar Poiseuille flow between two infinite parallel plates separated by a distance H . The CFD results are extracted at a location downstream where the flow is fully-developed (i.e. no longer varying in the streamwise direction x), and are compared with the expected behaviours obtained from the numerical solution of the equations for steady-state shear flow (which here varies in the y -direction) presented in Section 3.2.

In contrast with the case of the Couette flow presented previously, the shear-rate for a Poiseuille flow increases from the centreline to the walls and is only maintained constant on y -planes along the streamwise direction (so the flow is viscometric and steady shear but not homogeneous [75]). Thus, the necessity to use the effective Weissenberg number in Eqs. (5), (16) and (17), instead of a characteristic Wi when investigating generalised flows becomes obvious. For this type and for more general flows, Wi^{eff} can be considered as a local Weissenberg number. The local value of Wi^{eff} has to be evaluated at every computational cell in order to take into account the local stretching and therefore to evaluate the response of the stresses of the ALS-C model.

Fig. 9 illustrates the obtained contour-plots at steady-state when $Wi = 10$ for two different values of z , while $s = 1$. In particular, Fig. 9(a)–(c) show the solutions obtained for the effective Weissenberg number, b_s and A_{11} respectively when $z = 1$ in Eq. (16) (or Eq. (1)), while in Fig. 9(d)–(f) the equivalent solutions for $z = 4$ are provided. For both cases Wi^{eff} is the same and, as expected, is zero along the centreline (due to symmetry, $\dot{\gamma}$ is identically zero here) and increases at locations closer to the walls (Fig. 9(a) and (d)). In Fig. 9(b) and (e) the different behaviours for b_s for different z values is clearly shown.

When $z = 1$, b_s remains equal to b_m only for a very small region around the centreline in contrast to the case of $z = 4$, while as we move closer to the walls for both cases b_s starts to deviate from b_m . As expected, this affects the behaviour of the developed stresses, with the behaviour being illustrated in Fig. 9(c) and (f) in terms of the dominant first diagonal element (A_{11}) of the conformation tensor. It is noted that in a fully-developed channel flow the difference of the transverse normal stresses τ_{22} and τ_{33} must be zero (the ALS-C model, like the FENE-P model predicts $N_2 = 0$ in steady shear flow [76]), while as Wi increases then TrA tends to reach the maximum extensibility of the molecule ($TrA \rightarrow L^2$). Considering Eq. (8) of the ALS-C model (and the equivalent Eq. (9) of FENE-P) A_{22} and A_{33} will asymptotically reach zero in order to balance the increase of TrA .

Fig. 10 illustrates in a similar way the obtained contour-plots at steady-state when $Wi = 10$ for two different values of s , while $z = 1$. Fig. 10(a)–(c) show the solutions obtained for Wi^{eff} , b_s and A_{11} when $s = 0.5$ in Eq. (3), while in Fig. 9(d)–(f) the equivalent solutions for $s = 2$ are provided. Similar conclusions and responses to what was observed above can be seen for all the presented variables. What is worth noting is that for these two cases the effects of the s parameter on Wi^{eff} are now obvious since s is modifying its magnitude.

A more quantitative comparison of b_s and A_{11} obtained by CFD is given in Fig. 11 for the two cases. The CFD results are plotted against the predicted behaviour from the numerical solution of the model equations when in steady-state shear flow. As can be seen, the solutions obtained are in an excellent agreement both for the actual extensibility (see Fig. 9(a)) and for the first diagonal element of the conformation tensor (see Fig. 9(b)).

In Appendix A.2 a discussion illustrating the issues that need to be addressed when the original formulation proposed in Ghosh et al. [45] is employed is provided. In particular, the original formulation appears to have important inconsistencies for a flow inside a channel. Moreover, an additional case of a flow around a 90° channel bend at different geometrical angles is given, further supporting the case that the original formulation is not appropriate for complex flows and demonstrating the robustness of our modified approach.

4.2. Planar 4:1 contraction flow

Here we investigate the behaviour of dilute polymer solutions with $\beta = 0.90$ and $\beta = 0.95$ modelled with the ALS-C model for a flow within a planar two-dimensional 4:1 contraction. This problem is a well-known benchmark in computational rheology [21,77]. Three different values of maximum extensibilities have been considered: $b_m = 300$, $b_m = 1500$ and $b_m = 5000$, while for some cases the effects of varying z and s

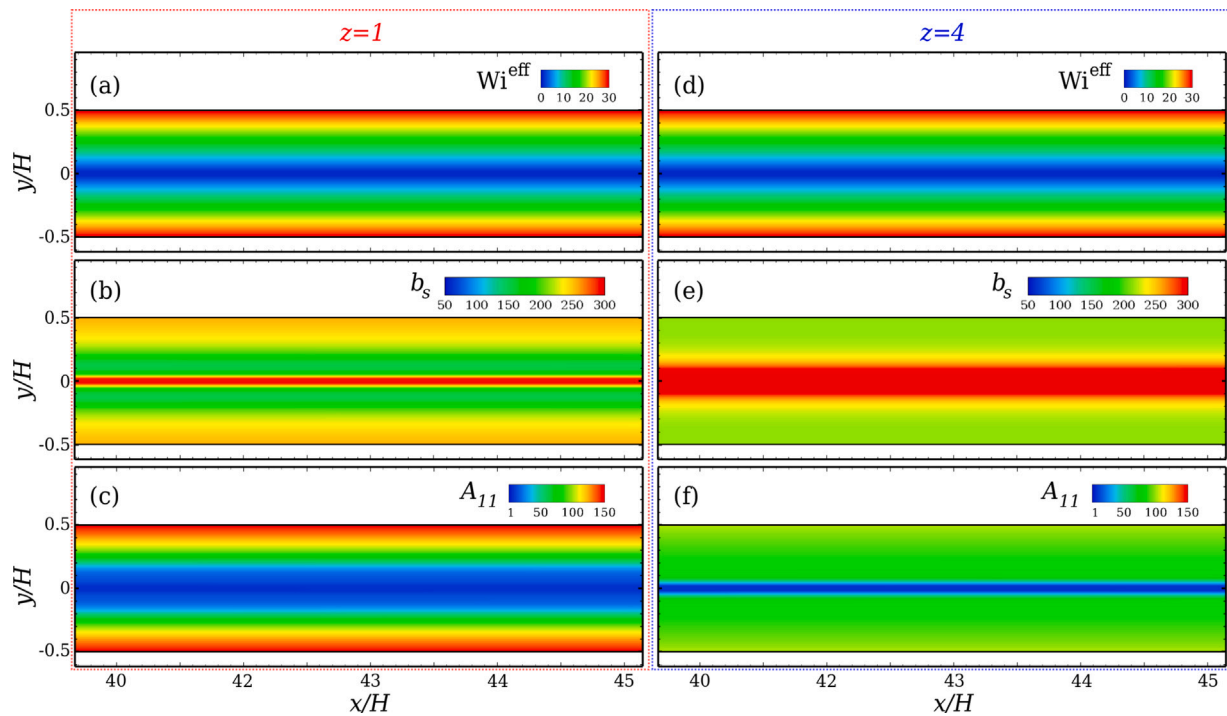


Fig. 9. Contour-plots of the ALS-C model for $b_m = 300$ and $s = 1$ illustrating the (a, d) Wi^{eff} , (b, e) b_s and (c, f) A_{11} for different values of z in Eq. (16). (a–c) correspond to the case of $z = 1$ and (d–f) to $z = 4$.

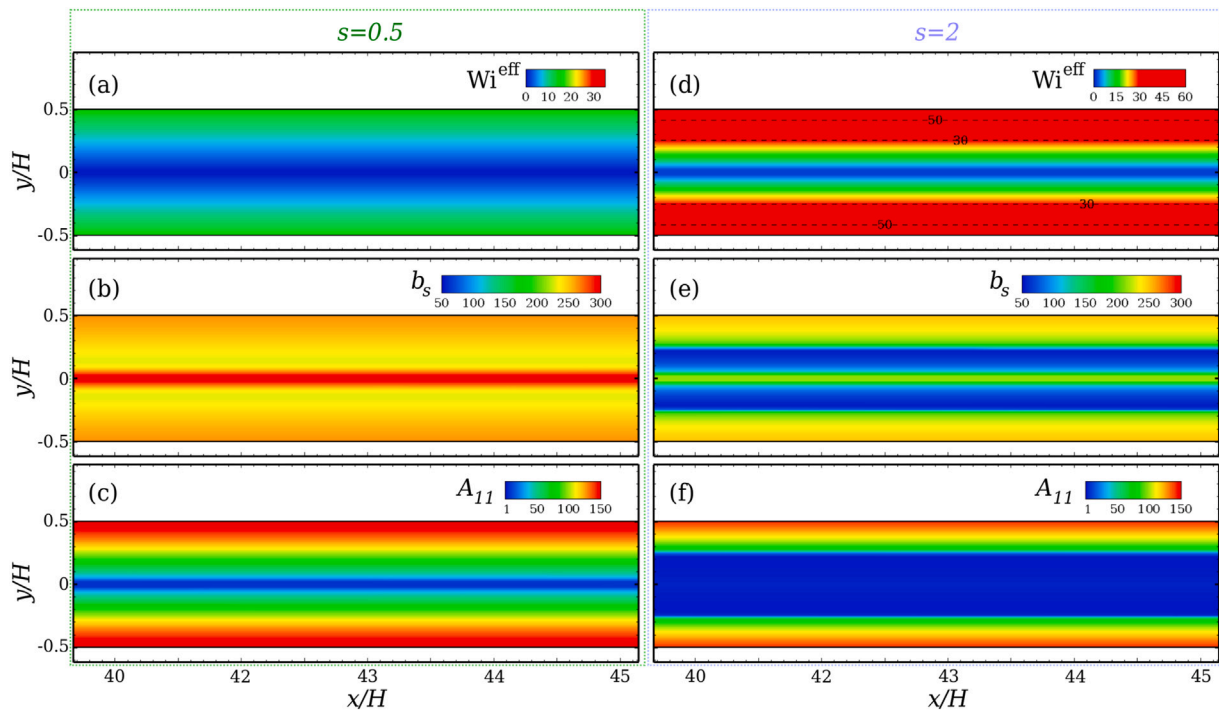


Fig. 10. Contour-plots of the ALS-C model for $b_m = 300$ and $z = 1$ illustrating the (a, d) Wi^{eff} , (b, e) b_s and (c, f) A_{11} for different values of s in Eq. (3). (a–c) correspond to the case of $s = 0.5$ and (d–f) to $s = 2$. The dashed-lines in (d) correspond to constant Wi^{eff} values.

parameters are reported. The characteristic Weissenberg number of the problem is defined as $Wi = \lambda U/H$, where H is the half width of the outlet channel and U is the average velocity developed within (see Fig. 12). The numerical mesh employed is illustrated in Fig. 12, while more details for all the meshes considered are provided in Table 1. These meshes are similar in density to the meshes M4 and M5 used in

Alves et al. [77]. All simulations are performed considering symmetry boundary conditions along the geometry centreline ($y/H = 0$).

4.2.1. Kinematics and flow fields

In this section the kinematics produced by the ALS-C model are presented and the results are juxtaposed with the equivalent responses

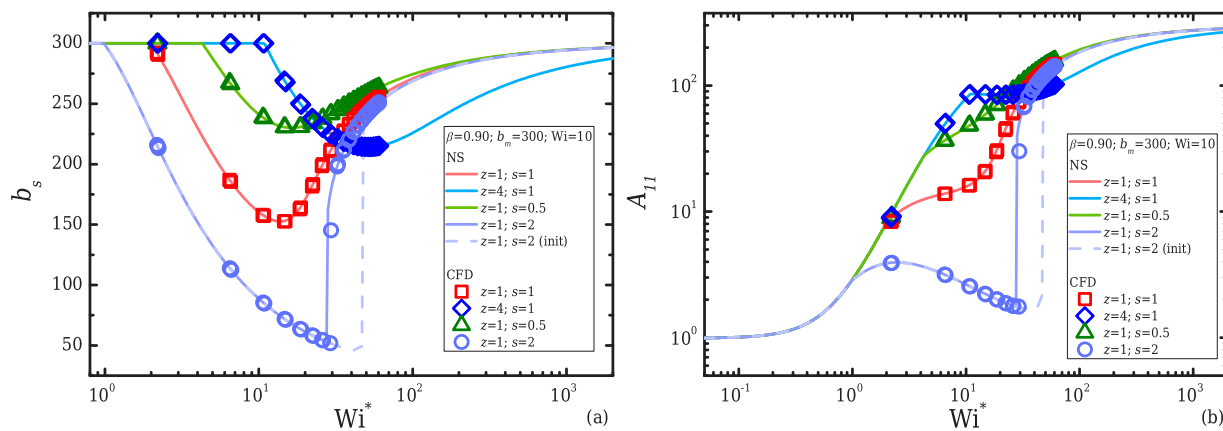


Fig. 11. Behaviour of (a) b_s and (b) A_{11} when $Wi = 10$, for the ALS-C model when $b_m = 300$ for all the cases of examined as a function of Wi^* . The responses obtained from the CFD simulations are compared with the predicted behaviour of the model when in steady-shear flow.

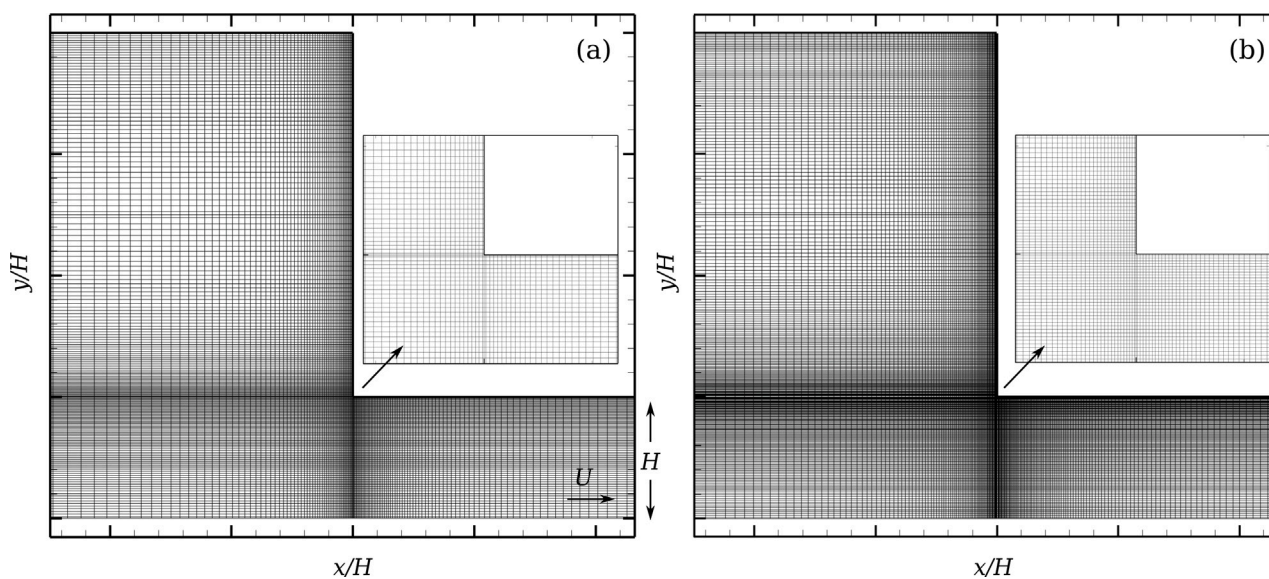


Fig. 12. Numerical grids employed for the study of a 4:1 contraction geometry: (a) M1; (b) M2.

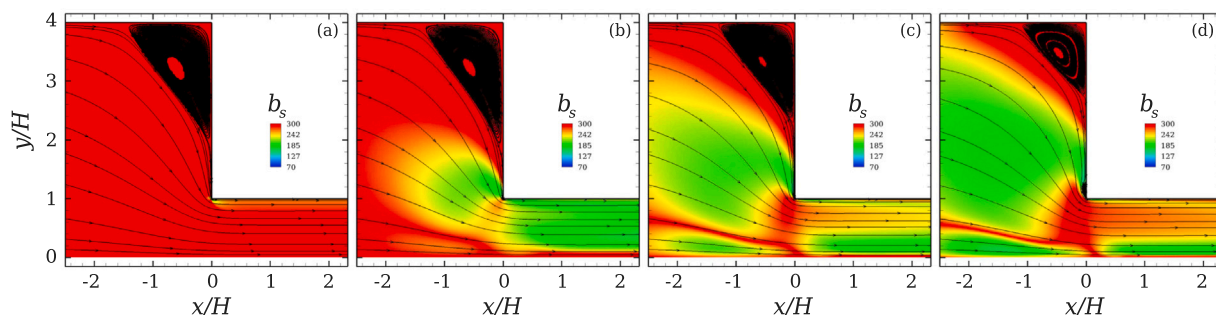


Fig. 13. Contours of b_s with superimposed streamlines in a 4:1 contraction flow when (a) $Wi = 1$, (b) $Wi = 10$, (c) $Wi = 20$ and (d) $Wi = 30$ for a dilute polymer solution with $\beta = 0.90$, $b_m = 300$, $z = 1$ and $s = 1$.

of the FENE-P model to highlight their differences. For all the cases discussed here considering the ALS-C model the z and s parameters are set equal to unity, with their effects investigated in the following section. In Fig. 13 the obtained fields for b_s are provided for different characteristic Weissenberg numbers. The illustrated contours are superimposed by the streamlines of the velocity field within the 4:1 contraction. When $Wi = 1$ (Fig. 13(a)), it can be seen that b_s is mostly

maintained equal to b_m , since the local Weissenberg number (Wi^*) is low. Around the corner, and where Wi^* (and Wi^{eff}) is increased, some deviations from b_m are produced. As Wi increases (see Fig. 13(b)–(d)) the deviations from b_m become more pronounced both at the developing region around the contraction but also downstream since the local Weissenberg is higher in the downstream channel compared to the upstream. Furthermore, it can be seen that after $Wi = 20$, the

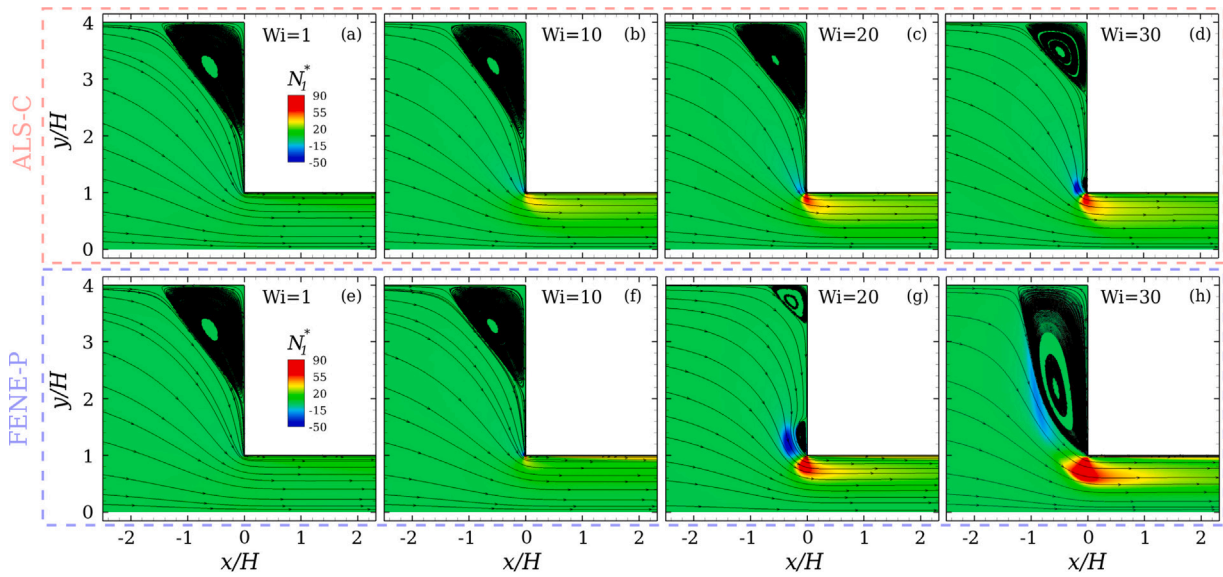


Fig. 14. Contours of $N_1^* = (\tau_{11p} - \tau_{22p})/(\eta_p U/H)$ with superimposed streamlines in a 4:1 contraction flow for the (a–c) ALS-C with $z = 1$, $s = 1$ and $b_m = 300$, and (d–f) FENE-P, for a dilute polymer solution with $\beta = 0.90$.

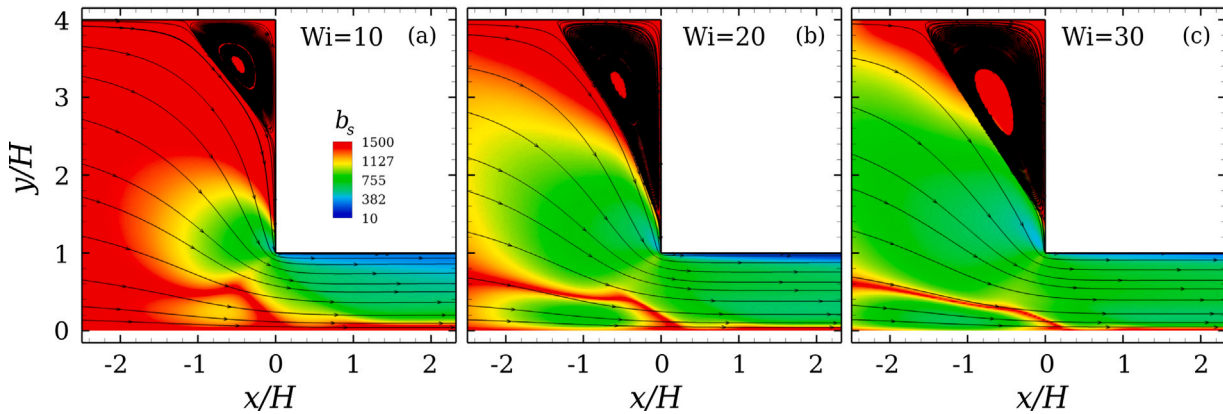


Fig. 15. Contours of b_s with superimposed streamlines in a 4:1 contraction flow when (a) $Wi = 10$, (b) $Wi = 20$ and (c) $Wi = 30$ for a dilute polymer solution with $\beta = 0.90$, $b_m = 1500$, $z = 1$ and $s = 1$.

Table 1
Characteristics of the numerical meshes employed for discretising the 4:1 contraction geometry.

Mesh	$\delta x_{min}/H$	$\delta y_{min}/H$	#Computational cells
M1	~ 0.007	~ 0.007	47,628
M2	~ 0.005	~ 0.005	91,952

corner vortex reduces in size and a lip vortex starts to form. The latter is more distinguishable at $Wi = 30$. Extracting transverse profiles of b_s and A_{11} at locations downstream of the contraction and where the flow is fully-developed for all the investigated cases, the obtained solutions are in a perfect agreement with the numerical solutions at steady-state shear flow (not shown for conciseness).

Fig. 14 illustrates the contours of the normalised polymeric part of the first normal-stress coefficient, $N_1^* = (\tau_{11p} - \tau_{22p})/(\eta_p U/H)$, superimposed with streamlines for a dilute polymer solution with $\beta = 0.90$, modelled by the ALS-C model when $b_m = 300$, in contrast to the equivalent behaviour generated by the FENE-P model with $L^2 = 300$ (alternative representations of streamlines and N_1 fields can be found in López-Aguilar and Tamaddon-Jahromi [78]). Solutions of the obtained fields are almost the same for low Wi , but it can be seen that as Wi increases the responses are different. The generated first normal-stress

differences are lower for the ALS-C model with the formation of the lip vortex being delayed in contrast to the FENE-P model, for which at $Wi = 30$ the lip is merged already with the corner vortex. Fig. 15 illustrates the field of b_s around the 4:1 contraction with superimposed streamlines for three different characteristic Weissenberg numbers for a dilute polymer solution with $\beta = 0.90$, $b_m = 1500$ and $z = 1$. It can be seen that as before, b_s has larger deviations from b_m and the intensity of the corner vortex increases with increasing Wi . It is interesting at this point to note that as in the previous case of $b_s = 300$, a thin region where $b_s = b_m$ is formed when $Wi \geq 20$, located at $y/H \lesssim 1$. It was found that this behaviour is caused by the fact that the magnitude of the outer product in Eq. (5) goes to zero. Having a zero magnitude means that the two normalised vectors of Eq. (5) are aligned and thus, the area formed between them is zero. Following the ideas anticipated in Ghosh et al. [45], this means that along this path the molecular stiffening, which is related to the angle of the molecule with the applied stretching, is zero.

In Fig. 16 a comparison of the obtained behaviour for b_s (Fig. 16(a)) and A_{11} (Fig. 16(b)) between CFD and the numerical solution for a steady-state shear flow is given, for all the Weissenberg numbers examined. The CFD profiles are taken at a location downstream of the contraction where the flow is fully-developed. Up to $Wi = 20$ the solution obtained is matching very well with the expected response. For

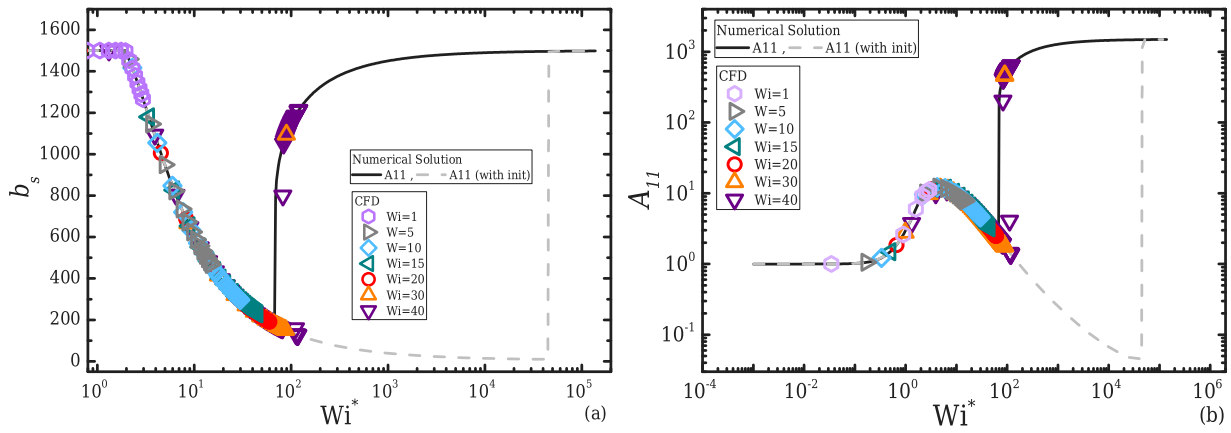


Fig. 16. Transverse profiles of (a) b_s and (b) A_{11} downstream of the flow and where it is fully-developed, for the ALS-C model with $b_m = 1500$ and $z = 1$ for increasing Wi^{eff} at different characteristic Weissenberg numbers. The responses are compared with the predicted behaviour of the model when in steady-shear flow. The dashed-line corresponds to the obtained behaviour when during the numerical solution for each case the values obtained at previous Wi are used as an initialisation.

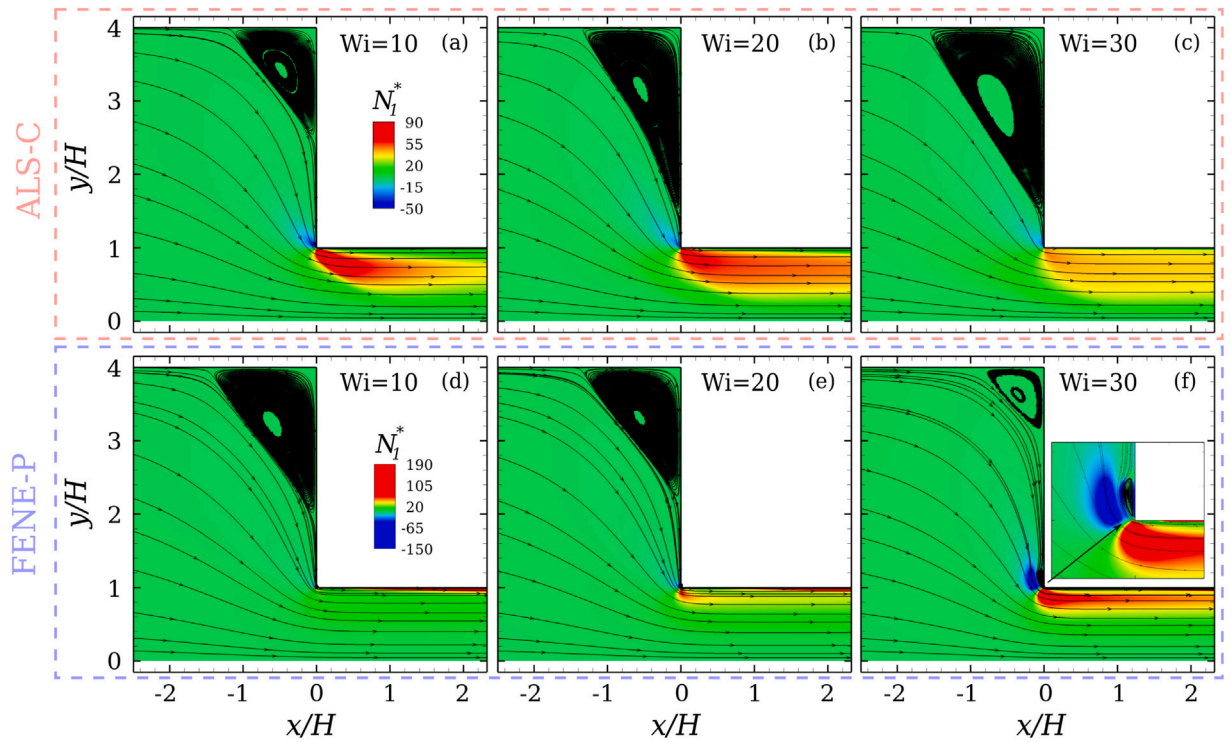


Fig. 17. Contours of $N_1^* = (\tau_{11p} - \tau_{22p})/(\eta_p U/H)$ with superimposed streamlines in a 4:1 contraction flow for the (a-c) ALS-C with $z = 1$ and $b_m = 1500$, and (d-f) FENE-P, for a dilute polymer solution with $\beta = 0.90$.

larger values of $Wi = 30$ and $Wi = 40$, it can be seen that a bifurcating behaviour occurs around $Wi^* \sim 70$. This behaviour illustrates that the ALS-C model for this particular combination of z and b_m values has more than one solution branch. As mentioned in Section 3.2, the second solution was found by considering as an initialisation for each set of b_s and A_{ij} those sets that were obtained at a previous Wi^{eff} . If no initialisation is considered, the branch of the solution indicated by the solid-line is obtained, for which b_s is advancing towards b_m around $Wi^* \sim 70$. On the contrary, when the initialisation is considered, b_s is found to jump at $b_m = 1500$ when $Wi^* \sim 5 \times 10^4$. In Appendix D it is shown that this behaviour depends on the chosen values of z and b_m and ceases to exist after a specific set of values (e.g. it was not observed for any z value chosen when $b_m = 300$), similar to what was seen in Section 3.2 beyond a specific value of s . In general terms we noticed that as z increases or s decreases this behaviour is lost and a single solution exists.

In Fig. 17 a comparison between the ALS-C model with $z = 1$ (top-row; Fig. 17(a)–(c)) and the FENE-P (bottom-row; Fig. 17(d)–(f)) models for $\beta = 0.90$ and $b_m = L^2 = 1500$ is provided. The contours correspond to N_1^* and are superimposed with the streamlines of the flow field. It can be seen that for this particular case, N_1^* is more diffuse for the ALS-C model with its intensity decreasing as Wi increases. In contrast for the FENE-P model, for these particular Weissenberg numbers examined, the opposite behaviour occurs. Furthermore, for the ALS-C model the corner vortex is increasing in size without any lip-vortice being developed, a behaviour that has also been observed in other studies of viscoelastic fluid flows using the simplified version (linear and exponential) of the sPTT model [17,77,79], while for the FENE-P at $Wi = 30$ a lip vortex clearly is generated illustrating the range of different responses that can be captured.

At this point it is useful to examine the differences in kinematics between the ALS-C and FENE-P models by looking at the generated

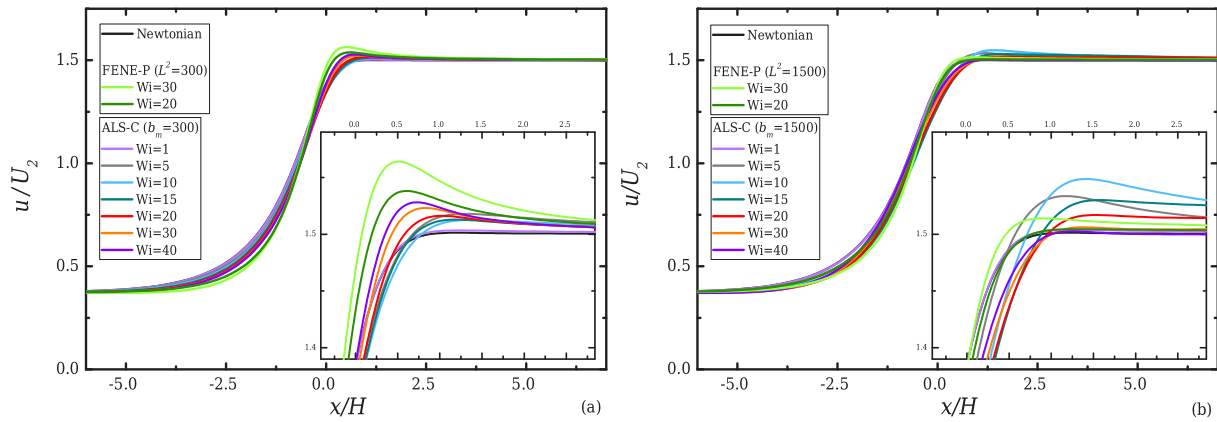


Fig. 18. Normalised streamwise velocity profiles along the flow centreline for dilute polymer solutions with $\beta = 0.90$ for the ALS-C model when $s = 1$ and $z = 1$ with (a) $b_m = 300$ and (b) $b_m = 1500$ for increasing Wi . The responses of the equivalent cases modelled by the FENE-P model are included at $Wi = 20$ and $Wi = 30$. The inset figures in both plots are zoomed versions at the velocity overshoot region.

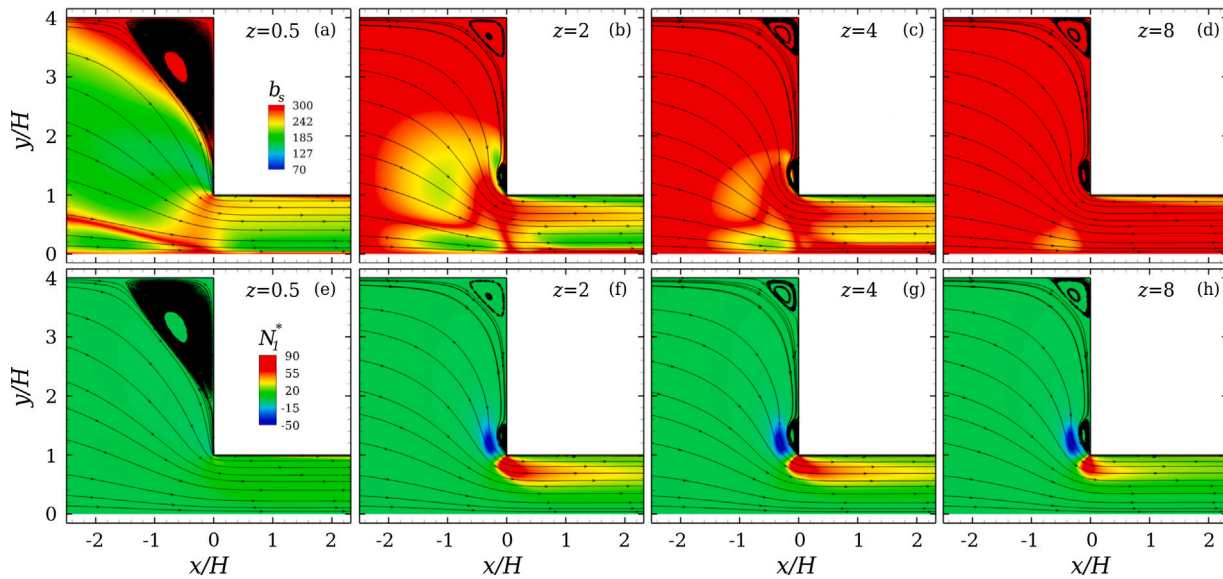


Fig. 19. Contours of b_s with (a) $z = 0.5$, (b) $z = 2$, (c) $z = 4$ and (d) $z = 8$ and the normalised first normal-stress difference when (e) $z = 0.5$, (f) $z = 2$, (g) $z = 4$ and (h) $z = 8$, with superimposed streamlines in a 4:1 contraction flow for a dilute polymer solution with $\beta = 0.90$, $b_m = 300$ and $s = 1$. For the case of $z = 2$ the simulations start to be unsteady and the contours are a time snapshot.

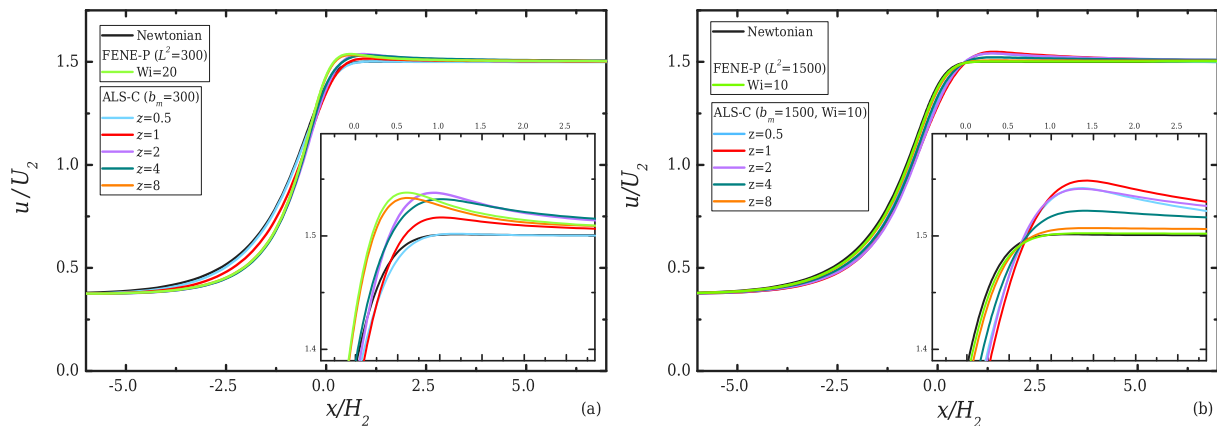


Fig. 20. Normalised streamwise velocity profiles along the flow centreline for dilute polymer solutions with $\beta = 0.90$ and $s = 1$ for different values of z for the ALS-C model with (a) $b_m = 300$ and (b) $b_m = 1500$ at $Wi = 20$ and $Wi = 10$ respectively. The responses of the equivalent cases modelled by the FENE-P are included for comparison. The inset figures in both plots are zoomed versions at the velocity overshoot region. For the case of $b_m = 300$ and $z = 2$ the simulations start to be unsteady.

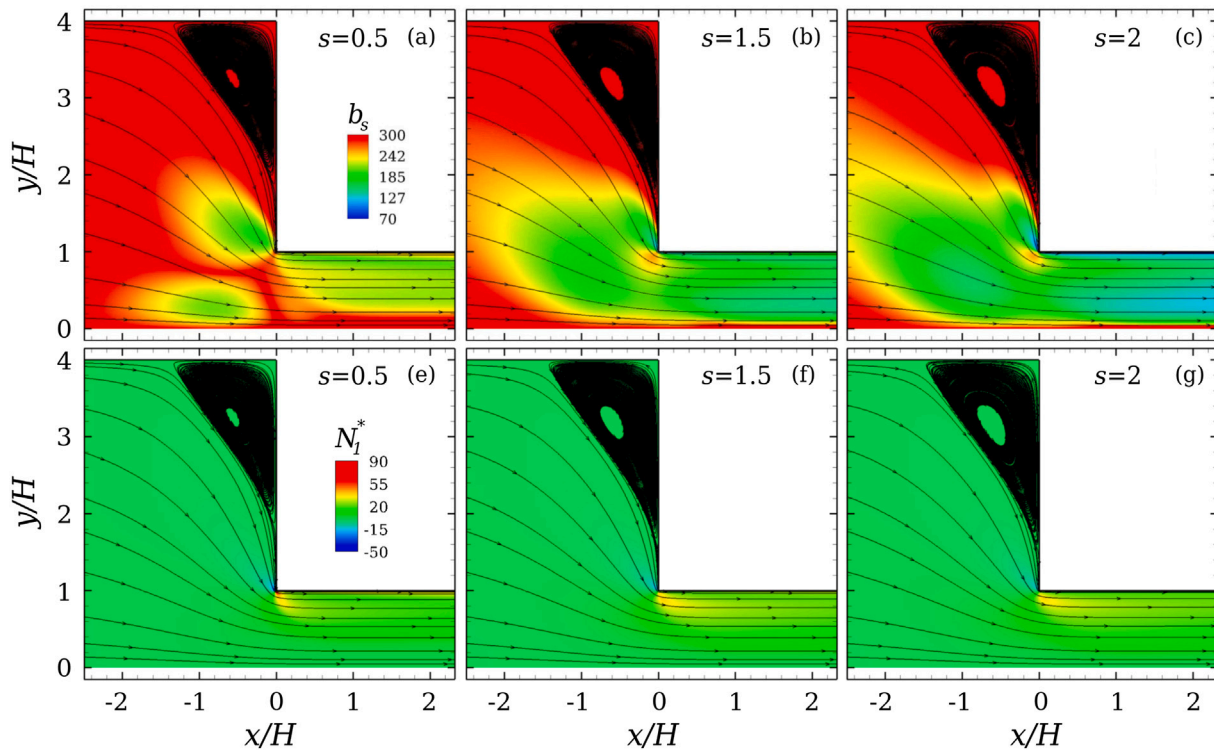


Fig. 21. Contours of b_s with (a) $s = 0.5$, (b) $s = 1.5$, (c) $s = 2$ and the normalised first normal-stress difference when (e) $s = 0.5$, (f) $s = 1.5$, (g) $s = 2$, with superimposed streamlines in a 4:1 contraction flow for a dilute polymer solution with $\beta = 0.90$, $b_m = 300$ and $z = 1$ at $Wi = 10$.

velocity profiles along the flow centreline. In Fig. 18, the obtained normalised velocity profiles are illustrated for the cases of $b_m = L^2 = 300$ and $b_m = L^2 = 1500$ (Fig. 18(a)). In Fig. 18(a), the former case is shown and it can be seen that a non-monotonic behaviour is observed for the ALS-C model as Wi increases. At low Wi , the velocity developed is similar to that of a Newtonian fluid flow, while at $Wi = 5$ an overshoot is seen to form. At $Wi = 10$ and $Wi = 15$ the obtained profiles are found to have smaller overshoots and start to approach the equivalent FENE-P results when the Weissenberg number increases further at $Wi = 20$. A similar response is also seen for the case of $b_m = L^2 = 1500$ shown in Fig. 18(b). It can be seen that the maximum velocity overshoot forms when $Wi = 10$ and for further increases the profile gets smaller values, shifting eventually towards the FENE-P response.

4.2.2. Influence of z -parameter

In this section, we report the influence of the z parameter (Eq. (1)) on the flow kinematics for fixed $s = 1$, for the particular cases of $b_m = L^2 = 300$ and $b_m = L^2 = 1500$ when $\beta = 0.90$ at $Wi = 20$ and $Wi = 10$ respectively. Fig. 19 illustrates the different responses obtained in terms of b_s (Fig. 19(a)–(d)) and in terms of N_1^* (Fig. 19(e)–(g)) when $b_m = 300$. It can be seen that for low values of z , b_s exhibits large deviations from b_m (or L^2) in the development region due to entrance effects around the contraction. As z increases, the ALS-C model starts to exhibit similar behaviour to the FENE-P model, with b_s exhibiting only mild deviations from b_m . Furthermore, differences in the corner vortex and the N_1^* are also clear. Comparing also with Fig. 14, it can be seen that for low z values the corner vortex is large and starts to decrease as z increases, while at the same time the lip-vortex becomes more pronounced (for $z = 1$ it is smaller), similar to what is observed for the equivalent case for the FENE-P model. Finally, as z increases N_1^* is also increasing, with the wider region of high N_1^* appearing when $z = 2$. In Appendix E, a comparison between the CFD results taken at a transverse profile downstream of the flow where the flow is fully-developed and the predicted responses at steady-state shear flows is provided illustrating their excellent agreement. Additionally,

the dependence of the second solution branch upon the choice of the z -parameter is shown.

In Fig. 20 the influence of z upon the velocity profiles is demonstrated, and compared with the equivalent solutions obtained for a Newtonian fluid and the FENE-P model. For both cases of $b_m = 300$ (Fig. 20(a)) and $b_m = 1500$ (Fig. 20(b)) the velocity overshoot is found to depend on the value of z , demonstrating a non-monotonic behaviour. In particular for the case of $b_m = 300$ the maximum overshoot occurs when $z = 2$, while for $b_m = 1500$ this occurs when $z = 1$. Additionally, for the case of $b_m = 300$ it can be seen that as z increases further than $z = 2$, the velocity overshoot decreases and then increases again to shift towards the behaviour observed for the FENE-P model.

4.2.3. Influence of s -parameter

In this section we report the behaviour of the ALS-C model when varying the s parameter while the z parameter is maintained fixed at $z = 1$. The cases investigated are for a dilute polymer solution with $\beta = 0.90$ while $b_s = 300$ and $b_s = 1500$. In Fig. 21 the behaviour of b_s and N_1^* with superimposed streamlines for the cases of $s = 0.5$, $s = 1.5$ and $s = 2$ is presented. As $s > 1$, then b_s becomes more diffusive in the entrance region. For this characteristic Weissenberg number there is no lip vortex forming at the corner of the contraction and only a corner vortex exist, while as s is increasing the latter gradually increases. On the contrary, the first normal-stress differences are slightly decreasing while s increases.

Fig. 22 shows the obtained solutions for increasing characteristic Weissenberg numbers for a dilute polymer solution with $\beta = 0.90$ when $s = 2$ and $b_m = 1500$. On the top row (Fig. 22(a)–(d)) the behaviour of b_s in the domain with superimposed streamlines is presented. For $Wi \geq 20$ the thin regions where \mathbf{n}_v and \mathbf{n}_A are aligned start to appear, and in contrast to the previous case shown in Fig. 15, they start to form upstream of the contraction after $x/H \leq -1$. The bottom row of Fig. 22 illustrates the development of N_1^* in the developing region for increasing Wi . Similar to all the responses seen so far, also for this case it can be seen that as Wi increases, N_1^* has a non-monotonic behaviour.

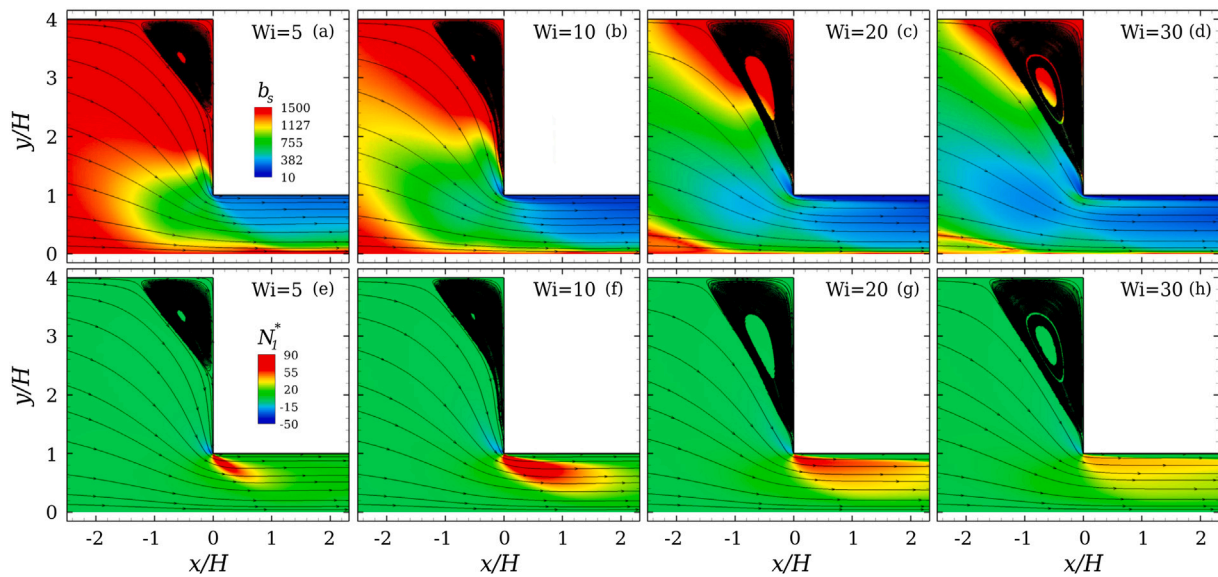


Fig. 22. Contours of b_s and the normalised first normal-stress difference when (a), (e) $Wi = 5$, (b), (f) $Wi = 10$, (c), (g) $Wi = 20$ and (d), (h) $Wi = 30$, with superimposed streamlines in a 4:1 contraction flow for a dilute polymer solution with $\beta = 0.90$, $b_m = 1500$, $z = 1$ and $s = 2$.

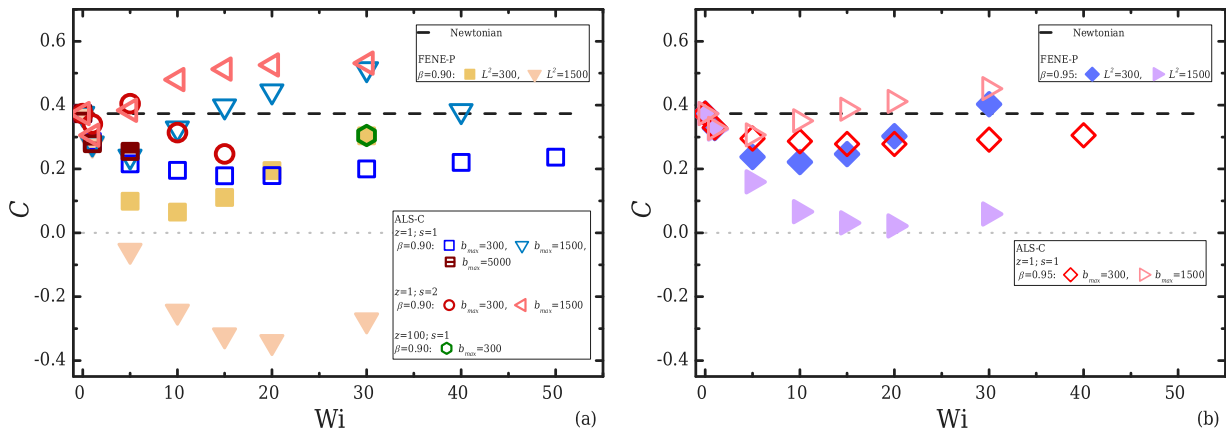


Fig. 23. Couette correction for dilute polymer solutions with (a) $\beta = 0.90$ and (b) $\beta = 0.95$, for the ALS-C with $b_m = 300$, $b_m = 1500$ and $b_m = 5000$ with $z = 1$ and $s = 1$ (open symbols). The cases with $z = 1$ and $s = 2$ for $\beta = 0.90$ and $b_m = 300$ and the specific case of $z = 100$, $s = 1$ when $\beta = 0.90$ and $b_m = 300$ for the ALS-C model are included. Additionally the responses of FENE-P for the same solutions when $L^2 = 300$ and $L^2 = 1500$, are provided for comparison (closed symbols). The *dashed line* indicates the Newtonian value, while the *dotted line* is a guide to the eye for the $C = 0$. Any *part-closed* symbols correspond to time-dependent flows.

The intensity of N_1^* starts to grow initially around the corner of the domain and then increases downstream of the corner up to $Wi = 20$. For further increases N_1^* starts to lose its intensity.

4.2.4. Pressure-drop measurements

In this section we present our results on the excess pressure-drop measurements caused by the contraction expressed in terms of the so-called Couette correction coefficient C [14,22,80]. The coefficient is defined as $C \equiv (\Delta P - \Delta P_{fd,U} - \Delta P_{fd,D})/2\tau_w$, where ΔP is the pressure-drop along the contraction, $\Delta P_{fd,U}$ and $\Delta P_{fd,D}$ are the pressure-drops upstream and downstream of the contraction where the flow is fully-developed and τ_w is the stress applied at the wall of the outlet channel where the flow is fully-developed, considering the fundamental relationship $\tau_w = \Delta P_{fd,D}H/L$ [14,22,80]. Defined in this manner, the Couette correction represents a non-dimensional form of the excess pressure drop solely due to the contraction.

In Fig. 23 the values of the Couette correction coefficient for all the investigated cases of dilute polymer solutions ($\beta = 0.90$ and $\beta = 0.95$) considered are presented. For clarity, the results are presented for those with $\beta = 0.90$ in Fig. 23(a) and for those with $\beta = 0.95$ are shown in Fig. 23(b). It can be seen that overall the model is not

able to predict large enhancements in pressure-drops compared to the Newtonian fluid case. However, depending on the case, it manages to predict higher values for C compared to the equivalent FENE-P cases, further supporting the idea that the use of a rate-dependent extensibility parameter is essential [81]. For those cases with $b_m = L^2 = 300$ it can be seen both in Figs. 23(a) and 23(b) that the ALS-C model initially predicts slightly higher values compared to the FENE-P model, eventually reaching a plateau that is then exceeded by the FENE-P model. Note that for this value of the maximum extensibility and when $z = 100$, the exact same value for C is obtained with the FENE-P model for the investigated case at $Wi = 30$ (further comparison of the obtained flow fields is given in Appendix D). This agreement further demonstrates the correct implementation of the CFD solver, since the expected behaviour that the ALS-C tends to the FENE-P in the limit of $z \rightarrow \infty$ is predicted. When changing the value of s , and in particular for the case of $\beta = 0.90$ with $s = 2$ and $b_m = 300$, it can be seen that an initial enhancement exists. However, further increases in Wi are not followed by further increases in C but rather result in a decrease in the evaluated pressure-drop. On the contrary when a high polymer extensibility is employed, $b_m = L^2 = 1500$, it can be seen that the ALS-C model predicts coefficients with larger differences

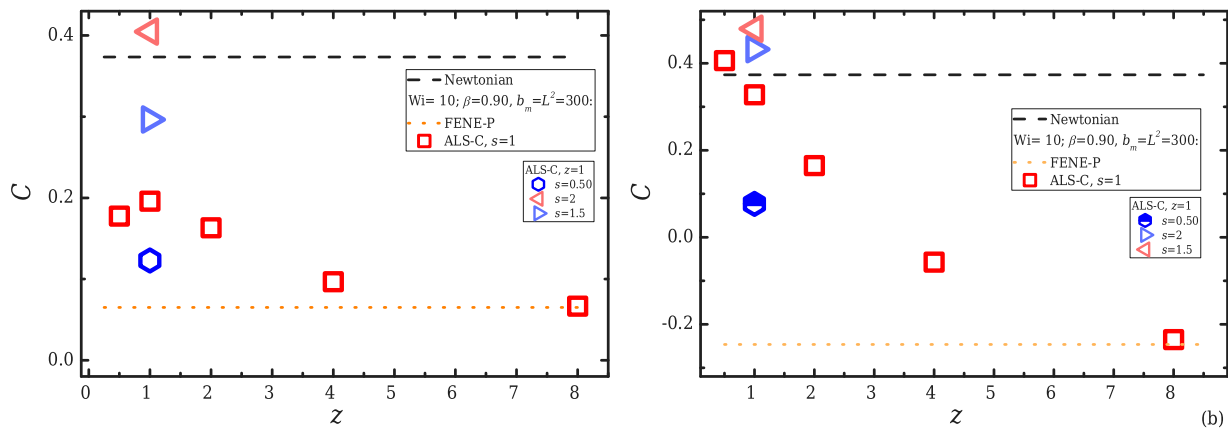


Fig. 24. Couette correction for dilute polymer solutions with $\beta = 0.90$ and different z values when (a) $b_m = 300$ and (b) $b_m = 1500$ and for different values of s when $z = 1$ at $Wi = 10$. Any *part-closed* symbols correspond to time-dependent flows. The *dashed line* indicates the Newtonian value, while the *dotted line* is a guide to the eye for the equivalent FENE-P case at the same Wi .

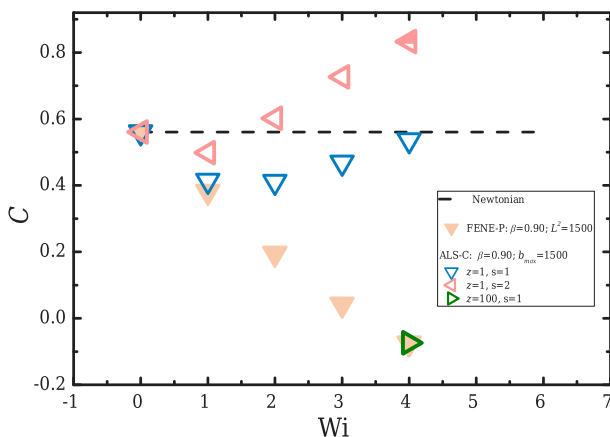


Fig. 25. Couette correction for dilute polymer solutions with $\beta = 0.90$ for the ALS-C model with $b_m = 1500$ and $z = 1$ for different values of the s parameter in an axisymmetric abrupt 4:1 contraction. The specific case of $z = 100$ at $Wi = 3$ for the ALS-C model is included. Additionally the responses of the FENE-P model for the same solution with $L^2 = 1500$ is provided for comparison. The *dashed line* indicates the Newtonian value, while any *part-closed* symbols correspond to time-dependent flows.

compared to the equivalent FENE-P cases for both β values considered, managing additionally to exceed the Newtonian value. In particular the FENE-P model under these conditions predicts a pressure recovery at high Wi (i.e. a negative Couette correction which is not observed in practice [14]). For the particular case of $s = 2$ with $z = 1$ when $\beta = 0.90$ it can be seen in Fig. 23(a) that an enhancement in pressure-drop exist at smaller Wi numbers.

To investigate further the capabilities of the model, the influence of the z and s parameters are reported in Fig. 24 for the cases of $\beta = 0.90$ with $b_m = 300$ and $b_m = 1500$. Fig. 24(a) shows the results for the case with $b_m = 300$. It can be seen that the maximum obtained value is obtained for $z = 2$. On the contrary for the case of $b_m = 1500$ shown in Fig. 24(b), the maximum obtained value is for $z = 0.5$. For both cases it can be observed that as the value of z is increasing, the solution obtained moves towards the FENE-P similarly to what it was reported and discussed in the previous sections. When the s parameter is increased further, increases in C are achievable managing to exceed the Newtonian value, with the case of $s = 2$ resulting in the higher enhancement at $Wi = 10$. However for $s < 1$, the evaluated C has lower values. It is clear that the ability of the ALS-C model to predict pressure drop enhancements is very sensitive to the choice of the model parameters.

Table 2

Comparison between the results obtained for the two meshes employed for a range of different cases.

Fluid	Wi	u/U_2	C
ALS-C ($\beta = 0.90, z = 1, s = 1$)			
$b_m = 300$	20	0.01%	0.09%
$b_m = 1500$	10	0.02%	0.33%

In order to verify that the results obtained are mesh independent, we illustrate in Table 2 the maximum deviations obtained between the velocity profiles at the overshoot peak and the Couette correction for each case when the meshes given in Table 1 are employed. The reported errors for all cases illustrate that the solutions obtained are in good agreement.

Before concluding this section it worth noting that we performed simulations considering the flow of dilute polymer solutions with $\beta = 0.90$ and $L^2 = 1500$ in an axisymmetric abrupt 4:1 contraction. As it can be seen in Fig. 25, the ALS-C model for with $z = 1$ and $s = 2$ predicts an enhancement in the Couette correction, while the case with $z = 1$ and $s = 1$ approaches the Newtonian value. On the contrary, as before, for the FENE-P model the values of the Couette correction are dropping as Wi increases. The case of the ALS-C model with $z = 100$ and $s = 1$ is also included and a very good agreement with the FENE-P model is found at $Wi = 4$.

5. Conclusions

In this paper we presented the set of equations that need to be implemented in order to employ the closed form of the Adaptive Length Scale (the ‘‘ALS-C’’) model in CFD simulations. We illustrated that a different procedure from the one used in Ghosh et al. [45] has to be followed for the results to be frame independent, incorporating the use of the normal unit vector of the conformation tensor. Additionally, a quadratic approximation for Eq. (1) was proposed to avoid the need to employ a more computational demanding root-finding method to solve for the instantaneous extensibility parameter. For steady-state shear flows the model was found, under certain conditions, to produce more than one solution branch for b_s and consequently for \mathbf{A} , depending on a combination of b_m, z and s , probably reflecting back to the employed closure.

It was illustrated that the ALS-C model is a generalisation of the FENE-P model maintaining the core ideas of the latter and introduces a new set of parameters that can be used for obtaining closer approximations to responses that are found experimentally. The basic modification is that the extensibility is allowed to vary depending

on the local characteristics of the flow field (Wi^{eff}). This behaviour was illustrated for several cases together with the influence it has on the kinematics. When $z \rightarrow \infty$ the behaviour of the FENE-P model is recovered (both in steady-state shear flows and CFD simulations in complex flows), while as Wi increases the behaviour of the ALS-C model asymptotes to the FENE-P response. For parameters that generate a different response, the ALS-C model manages to capture the pressure-drop enhancements for both cases of dilute polymer concentrations investigated. It is important to note that the steady-state extensional properties for the ALS-C and the FENE-P will be the same no matter the values of z and s (e.g. extensional viscosity, first normal-stress difference). Thus, from the results presented here, it is confirmed that the pressure-drop enhancement in contraction flows depends on non-steady state properties and these need to be captured by the constitutive model. In future work, we aim to provide direct comparison with experimental data to have a better insight of the actual capabilities of the model and to investigate more complex and three-dimensional geometries.

Declaration of competing interest

The authors declare that they have no known competing financial interests or personal relationships that could have appeared to influence the work reported in this paper.

Acknowledgements

KZ and RJP would like to express their deepest appreciation to Prof. Fernando Pinho and Prof. Manuel Alves for valuable help and discussions. Additionally, RJP and KZ would like to thank the EP-SRC, United Kingdom for the award of a fellowship under Grant No. EP/M025187/1.

Appendix A. Original approach of Ghosh et al. (2002)

The original approach proposed by Ghosh et al. [45] employs a different unit vector instead of \mathbf{n}_A in the outer product of Eq. (5), which is defined as

$$\mathbf{n}_C = \begin{pmatrix} (A_{11})^{1/2} \\ (A_{22})^{1/2} \\ (A_{33})^{1/2} \end{pmatrix} \frac{1}{(\text{Tr}\mathbf{A})^{1/2}}. \quad (\text{A.1})$$

In the following sections it will be shown that this approach appears problematic, as a consequence of frame invariance issues. Suggestions to overcome these issues are provided.

A.1. Steady-state shear flow

Considering the case of Section 3.2, the velocity profile is defined in Cartesian coordinates as $\mathbf{u} = (\dot{\gamma}_0 x_2, 0, 0)$, where $\dot{\gamma}_0$ is the constant shear-rate experienced by a fluid element along the x_2 direction. The shear-rate tensor for this velocity field will have the form:

$$\dot{\boldsymbol{\gamma}} = [\nabla\mathbf{u} + (\nabla\mathbf{u})^T] = \begin{bmatrix} 0 & \dot{\gamma}_0 & 0 \\ \dot{\gamma}_0 & 0 & 0 \\ 0 & 0 & 0 \end{bmatrix}. \quad (\text{A.2})$$

The three eigenvalues of the shear rate-rate tensor will be $\theta_1 = \dot{\gamma}_0$, $\theta_2 = -\dot{\gamma}_0$ and $\theta_3 = 0$, with their three corresponding normalised eigenvectors being $\mathbf{n}_{\dot{\gamma},1} = (1/\sqrt{2}, 1/\sqrt{2}, 0)$, $\mathbf{n}_{\dot{\gamma},2} = (1/\sqrt{2}, -1/\sqrt{2}, 0)$ ¹ and

¹ It is mentioned that for this eigenvector the signs between the non-zero elements can be reversed i.e. $\mathbf{n}_2 = (-1/\sqrt{2}, 1/\sqrt{2}, 0)$, however this does not affect the final result and the magnitude of $|\mathbf{n} \times \mathbf{n}_C|$ in Eq. (5) will be the same. This holds for a 2D flow, however in three dimensions differences of this type, although valid, are expected to introduce additional problems in the evaluation of the b_s evolution equation.

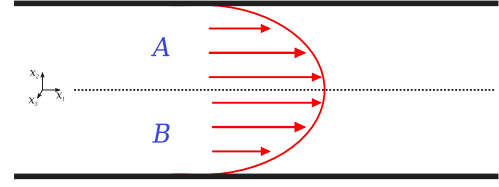


Fig. A.26. Schematic representation of a channel flow. The dotted line illustrates the location of the flow centreline.

$\mathbf{n}_{\dot{\gamma},3} = (0, 0, 1)$. As before, $\theta_3 = 0$ is a consequence of the 2D flow and is excluded, while the other two eigenvalues are, as expected, $|\theta_1| = |\theta_2|$ (see proof in Appendix B). From Eq. (2) the effective Weissenberg will be $Wi^{\text{eff}} = \lambda\dot{\gamma}_0/2$, irrespective of the choice of the eigenvalue. The evaluation of the outer product $|\mathbf{n}_{\dot{\gamma}} \times \mathbf{n}_C|$ in Eq. (5) considering each one of the normalised eigenvectors will give:

$$\begin{aligned} \theta_1 : |\mathbf{n}_{\dot{\gamma},1} \times \mathbf{n}_C| &= \left[C_{33}^2 + \frac{1}{2}(C_{22} - C_{11})^2 \right]^{1/2}, \\ \theta_2 : |\mathbf{n}_{\dot{\gamma},2} \times \mathbf{n}_C| &= \left[C_{33}^2 + \frac{1}{2}(C_{22} + C_{11})^2 \right]^{1/2}, \end{aligned} \quad (\text{A.3})$$

where $C_{ii} = (A_{ii}/\text{Tr}\mathbf{A})^{1/2}$ (the index $i = 1, 2, 3$ corresponds to each of the three directions and does not indicate Einstein summation). Comparing the two magnitudes it can be clearly seen that, although the absolute eigenvalues are the same, the choice of one eigenvector over the other will generate a different result for the magnitude of the outer product. The simplest solution to this may be to reject the case of the negative eigenvalue. However, we show below that this does not resolve the issue.

We now consider the reversed problem, for which the bottom wall is moving with a constant velocity and the top is fixed. The velocity field is described by the vector $\mathbf{u}^* = (\dot{\gamma}_0(H - x_2), 0, 0)$. It can be shown, that although the resulting shear-rate matrix has the same eigenvalues as seen in the previous case ($\theta_1^* = \theta_1 = \dot{\gamma}_0$, $\theta_2^* = \theta_2 = -\dot{\gamma}_0$ and $\theta_3^* = \theta_3 = 0$), the corresponding eigenvectors are not the same. In particular, and while considering only the non-zero eigenvalues, for the case of $\theta_1^* = \dot{\gamma}_0$ the corresponding eigenvector is now $\mathbf{n}_{\dot{\gamma},1}^* = (1/\sqrt{2}, -1/\sqrt{2}, 0)$, while for $\theta_2^* = -\dot{\gamma}_0$ we get $\mathbf{n}_{\dot{\gamma},2}^* = (1/\sqrt{2}, 1/\sqrt{2}, 0)$. Therefore, the evaluation of the outer product $|\mathbf{n}_{\dot{\gamma}} \times \mathbf{n}_C|$ will now give:

$$\begin{aligned} \theta_1^* : |\mathbf{n}_{\dot{\gamma},1}^* \times \mathbf{n}_C| &= \left[C_{33}^2 + \frac{1}{2}(C_{22} + C_{11})^2 \right]^{1/2}, \\ \theta_2^* : |\mathbf{n}_{\dot{\gamma},2}^* \times \mathbf{n}_C| &= \left[C_{33}^2 + \frac{1}{2}(C_{22} - C_{11})^2 \right]^{1/2}. \end{aligned} \quad (\text{A.4})$$

Comparing now Eqs. (A.3) and (A.4), it can be seen that although $\theta_1 = \theta_1^*$, $|\mathbf{n}_{\dot{\gamma},1} \times \mathbf{n}_C| \neq |\mathbf{n}_{\dot{\gamma},1}^* \times \mathbf{n}_C|$ (the same holds for $\theta_2 = \theta_2^*$). This demonstrates that simply choosing the positive eigenvalue (or the negative) is not adequate to ensure that results for this approach are frame independent. Thus, if the original equations of Ghosh et al. [45], proposed for homogeneous flows, are used unquestioningly in a general 3D solver it is likely that they will produce inconsistent results and potential numerical instabilities due to artificial symmetry-breaking etc. In fact we observed precisely such issues when we did implement the model following the original approach as is now discussed in Appendix A.2.

A.2. Channel flow

In this section the performance of the ALS-C model using the approach proposed in Ghosh et al. [45] (using Eq. (A.1) in Eq. (5) instead of \mathbf{n}_A) when simulating a channel flow is discussed. The analysis is for the same 2D channel employed in Section 4.1. Dividing the flow domain into two symmetric parts, A and B, as illustrated schematically in Fig. A.26 and expressing the shear-rate tensor exactly at two

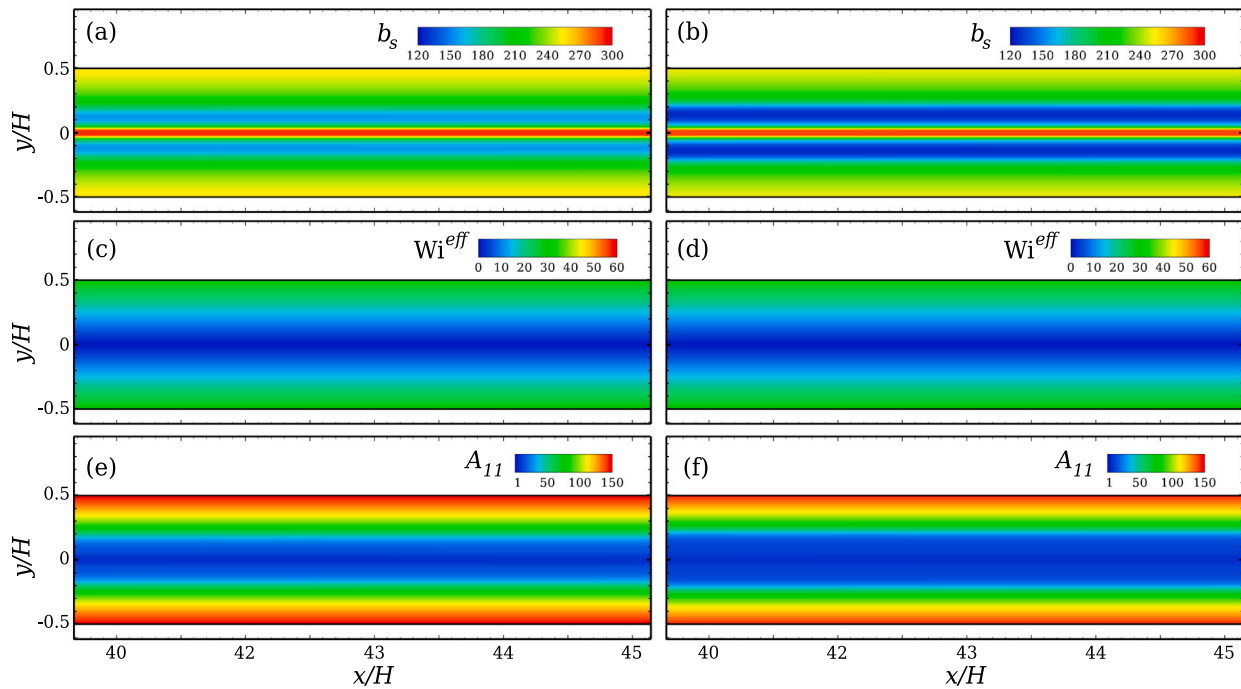


Fig. A.27. Contour-plots of the evaluated fields for (a, b) b_s , (c, d) Wi^{eff} and (e, f) A_{11} when $\mathbf{n}_{\gamma,1}$ and $\mathbf{n}_{\gamma,2}$ are used respectively while $b_m = 300$, $z = 1$ and $s = 1$.

arbitrary, but symmetric points of the flow field about the centreline we get:

$$\dot{\gamma}_A = \begin{bmatrix} 0 & -a & 0 \\ -a & 0 & 0 \\ 0 & 0 & 0 \end{bmatrix}, \quad \dot{\gamma}_B = \begin{bmatrix} 0 & a & 0 \\ a & 0 & 0 \\ 0 & 0 & 0 \end{bmatrix}, \quad (A.5)$$

where $a = \partial u_1 / \partial x_2$. As shown in Appendix B, the eigenvalues of matrices of this type will always be same in absolute value but with different signs. Thus, we can write that $\theta_{A,1} = \theta_{B,1} = a$ and $\theta_{A,2} = \theta_{B,2} = -a$. As reported before, it is straight forward to show that for the same eigenvalues the corresponding eigenvectors will be different and the inconsistency of the model is again clear. One of the eigenvectors will have both elements positive ($\mathbf{n}_{\gamma,1}$), while the other will have at least one negative ($\mathbf{n}_{\gamma,2}$). Therefore, if we choose to use the eigenvector in the outer product of Eq. (5) based only on the corresponding maximum eigenvalue (e.g. the positive value), the result will not be the same for a point at A and its symmetric counterpart at B . Therefore, the magnitude of the outer product in the evolution equation of b_s will be different for symmetric locations, which in turn will generate different stresses at points that should have the same flow characteristics via symmetry.

A solution to the problem would be to base our choice of the eigenvalue on a specific, more robust, criterion to enforce consistency. For example, examining the sign of the shear-rate at A this will be negative, while at B it will be the opposite. With that in mind, one could always choose the eigenvalue that has the same sign as the local shear-rate and that way the employed eigenvectors at symmetric locations will match. An alternative would be to base the choice on the opposite sign. In fact, this partially handles the problem. However, investigating flow conditions where streamwise gradients exist, the generated non-zero diagonal elements complicate the use of the eigenvectors at transition regions.

In Appendix C it is demonstrated that for a generic form of $\dot{\gamma}$ in 2D, a ‘‘flip’’ about the diagonal of the normalised eigenvector elements occurs depending on the sign of the shear-rate elements. Thus, the evaluation of the magnitude of the outer product will be problematic and will depend upon the flow direction. Typically, general flows have streamwise gradients and thus, the use of the original approach requires further modification. In fact, this inherent problem of the model can

also affect the simple flow in a channel. Considering the presence of a small numerical error in the diagonal elements of the shear-rate tensor (Eq. (A.2)), which prevents them for being identically zero, will result in the flip of the normalised vector elements at regions A and B . The differences between the flipped values are very small and its effects upon the outer product are not easily captured/identified. Clearly all these issues complicate the use of the model when simulating flows in 3D. To avoid the problem imposed by the direction sign of the shear elements we propose to evaluate everywhere the eigenvectors and eigenvalues of a modified shear-rate tensor, $\dot{\gamma}_m$, where the absolute values of the non-diagonal elements are considered:

$$\dot{\gamma}_m = \begin{bmatrix} \dot{\gamma}_{11} & |\dot{\gamma}_{12}| & |\dot{\gamma}_{13}| \\ |\dot{\gamma}_{21}| & \dot{\gamma}_{22} & |\dot{\gamma}_{23}| \\ |\dot{\gamma}_{31}| & |\dot{\gamma}_{32}| & \dot{\gamma}_{33} \end{bmatrix}. \quad (A.6)$$

The diagonal elements are maintained without absolute values since they must satisfy incompressibility and symmetric locations in a flow will not have opposite signs.

Fig. A.27 illustrates contour-plots of the obtained solutions for the 2D, fully-developed, flow in a channel when $Wi = 10$. In particular, Fig. A.27(a) and (b) show the solutions obtained for b_s when $\mathbf{n}_{\gamma,1}$ and $\mathbf{n}_{\gamma,2}$ are chosen respectively. For both cases b_s becomes equal to b_m within a small region along the flow centreline, due to the low values of Wi^{eff} . The evaluation of Wi^{eff} is illustrated in Fig. A.27(c) and (d) for each case respectively and it can be seen, that as expected, is increasing closer to the wall. While Wi^{eff} is increased, b_s starts to deviate from b_m . Finally, Fig. A.27(e) and (f) present the contour-plots of the first element of the conformation tensor, A_{11} . It can be seen that for the case of $\mathbf{n}_{\gamma,1}$ (positive eigenvector) it obtains slightly higher values overall compared to $\mathbf{n}_{\gamma,2}$. It can be seen that these responses are qualitatively the same with those reported in Section 4.1.

A more quantitative comparison of b_s and A_{11} obtained by CFD is given in Fig. A.28 for all cases. The CFD results are plotted against the predicted behaviour by the numerical solution of the model equations when in steady-state shear flow. It can be seen that for both eigenvectors, the solutions obtained are in good agreement both for b_s (see Fig. A.27(a)) and the elements of the conformation tensor (see Fig. A.27(b)).

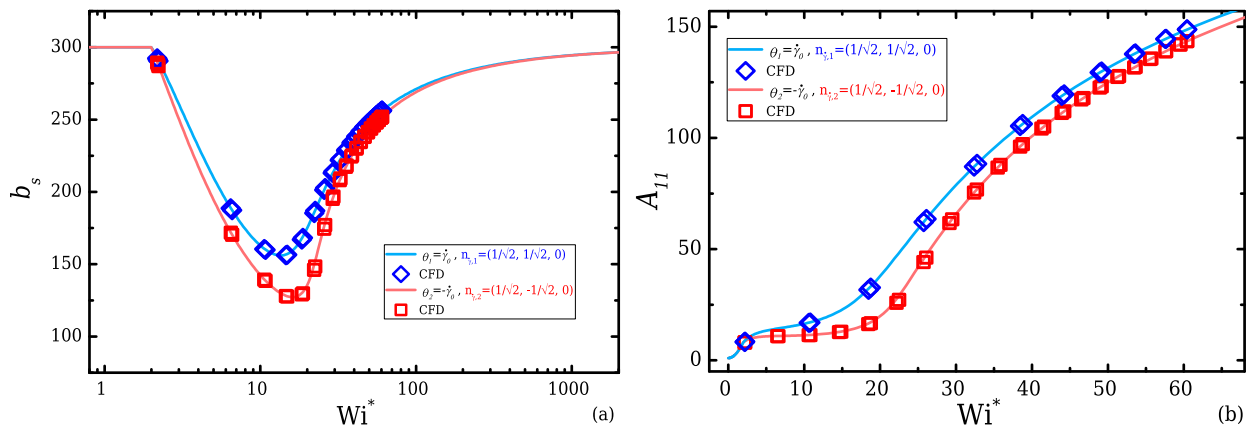


Fig. A.28. Behaviour of (a) b_s and (b) A_{11} when $\mathbf{n}_{z,1}$ and $\mathbf{n}_{z,2}$ are used, following the original approach of Ghosh et al. [45] for the ALS-C model with $b_m = 300$, $z = 1$ and $s = 1$ as a function of Wi^* . The responses obtained from the CFD simulations for a channel flow with $Wi = 10$ are compared with the predicted behaviour of the model when in steady-shear flow.

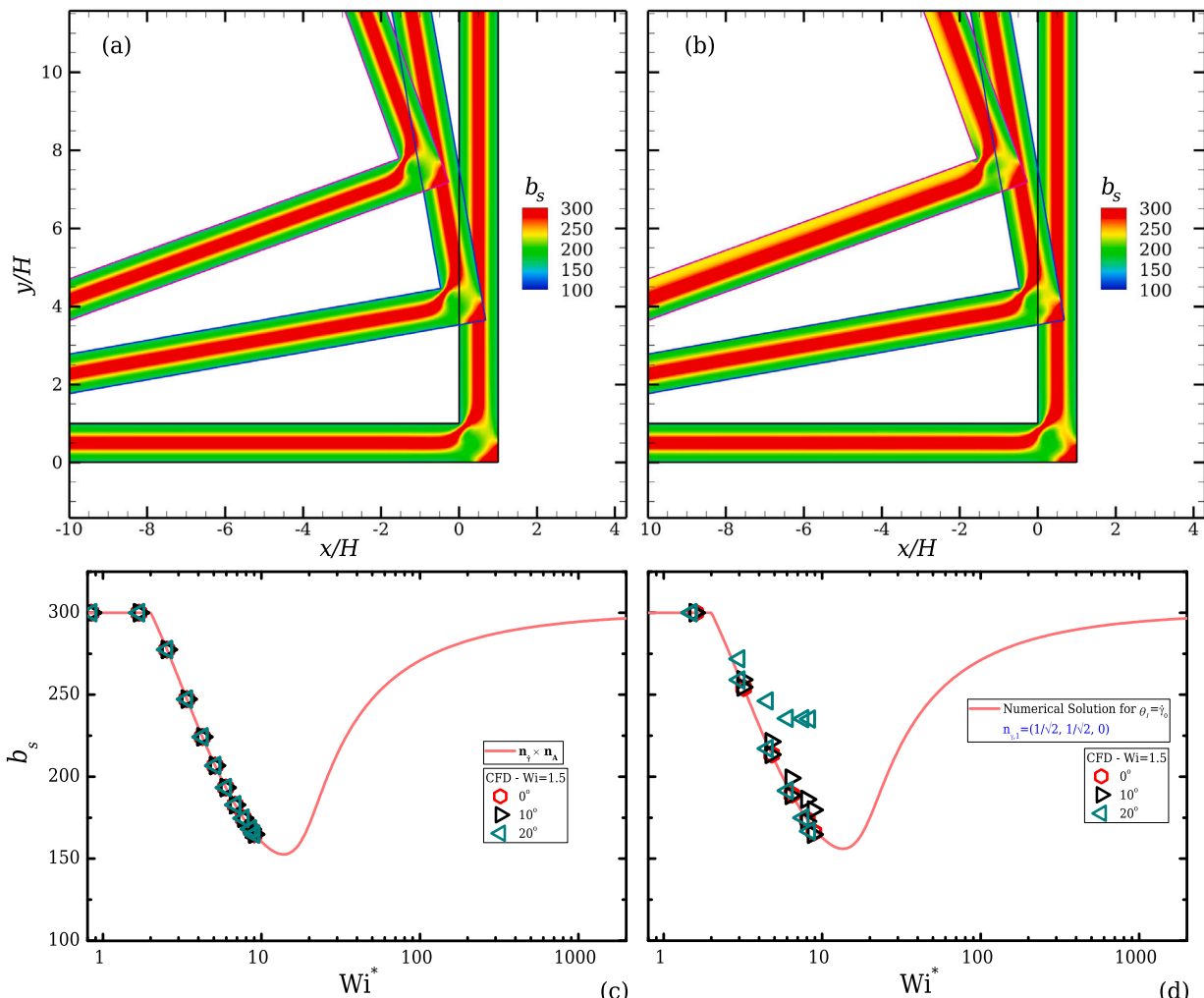


Fig. A.29. Contour-plot of the evaluated field for b_s when \mathbf{n}_A of Eq. (5) is (a) the eigenvector of the maximum eigenvalue of \mathbf{A} (as in Eq. (5)) and (b) defined as in Ghosh et al. [45] and discussed in Appendix A (Eq. (A.1)). In (c) and (d) the transverse profiles of each case respectively, extracted at a location upstream where the flow is fully-developed, are compared against the expected behaviour from steady-state shear flow for increasing Wi^* . All cases are for $b_m = 300$, $z = 1$ and $s = 1$.

A.3. Corner flow

Here we demonstrate a direct comparison between the two approaches for the outer product, employing a more complex flow via flow around a 90° channel bend. Following the discussion in Appendices A.1 and A.2, only the case of the eigenvector with positive

elements to represent the original approach in Ghosh et al. [45] is considered for comparison. Moreover, this case is investigated when different angles are applied in order to examine independence of the solution on the frame of the problem. In particular three cases are considered for each approach, employing geometries at 0° and rotated 10° and 20° relative to the x -axis (see Fig. A.29(a) and (b)).

The contours of Fig. A.29(a) and (b) present the obtained CFD solutions for b_s for a dilute polymer solution with $\beta = 0.90$ and $b_m = 300$ at $Wi = \lambda U/H = 1.5$, when the proposed approach (\mathbf{n}_A in Eq. (5)) and the original one suggested in Ghosh et al. [45], are used respectively. When the approach employed here is used, it can be seen that b_s contours are the same for all three different cases, exactly as should occur for a scalar quantity. This is additionally verified from the b_s profiles shown in Fig. A.29(c), taken at some point upstream of the inlet channel where the flow is fully-developed. For all cases, the profiles extracted match very well to one another and at the same time follow the expected behaviour from steady-state shear. On the contrary, when the approach used in Ghosh et al. [45] is considered, it can be clearly seen that the contours of the scalar quantity are affected by the imposed angle. The differences between the velocity and consequently the stress fields of the straight and tilted domains is affecting the evaluation of the actual extensibility. The normalised vector \mathbf{n}_C proposed by Ghosh et al. [45], is not able to contain all the information imposed by the applied rotation. This is further verified by the profiles taken at a location upstream of the inlet channel and presented in Fig. A.29(d), in which deviations from the expected response are clear. The case study presented here illustrates clearly that the methodology for using the ALS-C model in CFD simulations should be the approach presented in Section 2.1 expressed by \mathbf{n}_A . Employing directly the eigenvector of A which corresponds to its largest eigenvalue, instead of a normalised vector that is formed by its main diagonal elements (see Eq. (A.1)), ensures that the results will be frame independent since contributions from all directions are taken into account.

Appendix B. Eigenvalues for a general 2D flow

The shear-rate tensor for an arbitrary point in a 2D flow field will have the following form:

$$\dot{\gamma} = \begin{bmatrix} \dot{\gamma}_{11} & \dot{\gamma}_{12} & 0 \\ \dot{\gamma}_{21} & \dot{\gamma}_{22} & 0 \\ 0 & 0 & 0 \end{bmatrix}, \quad (B.1)$$

where $\dot{\gamma}_{11} = 2\partial u_1/\partial x_1$, $\dot{\gamma}_{22} = 2\partial u_2/\partial x_2$ and $\dot{\gamma}_{12} = \dot{\gamma}_{21} = \partial u_1/\partial x_2 + \partial u_2/\partial x_1$. The eigenvalues of the shear-rate tensor are found by solving $\det(\theta \mathbf{I} - \dot{\gamma}) = 0$:

$$\begin{vmatrix} \theta - \dot{\gamma}_{11} & -\dot{\gamma}_{12} & 0 \\ -\dot{\gamma}_{21} & \theta - \dot{\gamma}_{22} & 0 \\ 0 & 0 & \theta \end{vmatrix} = 0 \Rightarrow \theta[(\theta - \dot{\gamma}_{11})(\theta - \dot{\gamma}_{22}) - \dot{\gamma}_{12}^2] = 0 \quad (B.2)$$

Excluding the case of the zero eigenvalue ($\theta_3 = 0$) and by employing the incompressibility constraint $\nabla \cdot \mathbf{u} = 0$, from which $\partial u_1/\partial x_1 = -\partial u_2/\partial x_2$, Eq. (B.2) will produce, after some rearrangement, two equal eigenvalues in absolute terms, but with an opposite sign:

$$\theta_1 = \left[\left(2 \frac{\partial u_1}{\partial x_1} \right)^2 + \left(\frac{\partial u_1}{\partial x_2} + \frac{\partial u_2}{\partial x_1} \right)^2 \right]^{1/2},$$

$$\theta_2 = - \left[\left(2 \frac{\partial u_1}{\partial x_1} \right)^2 + \left(\frac{\partial u_1}{\partial x_2} + \frac{\partial u_2}{\partial x_1} \right)^2 \right]^{1/2}. \quad (B.3)$$

Appendix C. Example of non-zero diagonal elements

Here we demonstrate the ‘‘flip’’ of the elements of the eigenvectors at two symmetric points, occurring when Eq. (A.1) is employed instead of \mathbf{n}_A in Eq. (5). For simplicity a 2D example is provided. The matrices below represent the shear-rate tensor at two arbitrary, but symmetric points A and B in a flow field, where streamwise gradients also occur:

$$\dot{\gamma}_A = \begin{bmatrix} a & -a & 0 \\ -a & -a & 0 \\ 0 & 0 & 0 \end{bmatrix}, \quad \dot{\gamma}_B = \begin{bmatrix} a & a & 0 \\ a & -a & 0 \\ 0 & 0 & 0 \end{bmatrix}. \quad (C.1)$$

It can be seen that the diagonal elements satisfy continuity, while the off-diagonal elements have equal values in absolute terms, but different

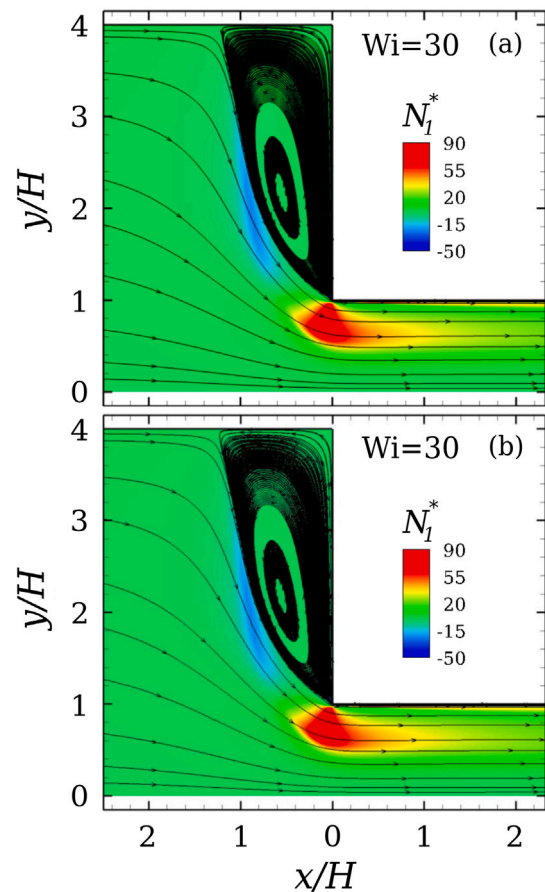


Fig. D.30. Contours of N_1^* with superimposed streamlines in a 4:1 contraction flow for the (a) ALS-C with $z = 100$ and (b) FENE-P for a dilute polymer solution with $\beta = 0.90$ and $b_m = L^2 = 300$.

signs due to the imposed direction. Evaluating the eigenvalues and the corresponding normalised eigenvectors for point A we find:

$$\theta_{A,1} = 1.41a : \quad \mathbf{n}_{A,1} = (0.924, 0.383, 0),$$

$$\theta_{A,2} = -1.41a : \quad \mathbf{n}_{A,2} = (-0.383, 0.924, 0), \quad (C.2)$$

$$\theta_{A,3} = 0 : \quad \mathbf{n}_{A,2} = (0, 0, 1)$$

Similarly, for point B we get:

$$\theta_{B,1} = 1.41a : \quad \mathbf{n}_{A,1} = (0.924, -0.383, 0),$$

$$\theta_{B,2} = -1.41a : \quad \mathbf{n}_{A,2} = (0.383, 0.924, 0), \quad (C.3)$$

$$\theta_{B,3} = 0 : \quad \mathbf{n}_{A,2} = (0, 0, 1)$$

The analysis done so far suggested that a solution to the inconsistency of the original approach proposed in Ghosh et al. [45] would be to set a criterion in order to use the same eigenvectors. A first choice would be to use the eigenvalue that has the same sign with that of the local shear rate. An alternative, but still consistent, would be to consider the opposite case. Comparing the eigenvectors in Eqs. (C.2) and (C.3), it can be seen that for a general point an its symmetric, none of these criteria will work. In particular, choosing the eigenvectors from $\theta_{A,1}$ and $\theta_{B,2}$, it can be seen that although both have positive elements their values are flipped, $\mathbf{n}_{A,1}^1 = \mathbf{n}_{B,2}^2$ and $\mathbf{n}_{A,1}^2 = \mathbf{n}_{B,2}^1$, with the superscript indicating the number of the element. Thus, the evaluation of the outer product in Eq. (5) will be different at point A and B . The same also occurs for the opposite choice of $\theta_{A,2}$ and $\theta_{B,1}$ which correspond to the eigenvectors that have at least one negative element.

The problem of approaching the ALS-C model in this manner, is that non-diagonal elements of the shear-rate tensor have a sign which

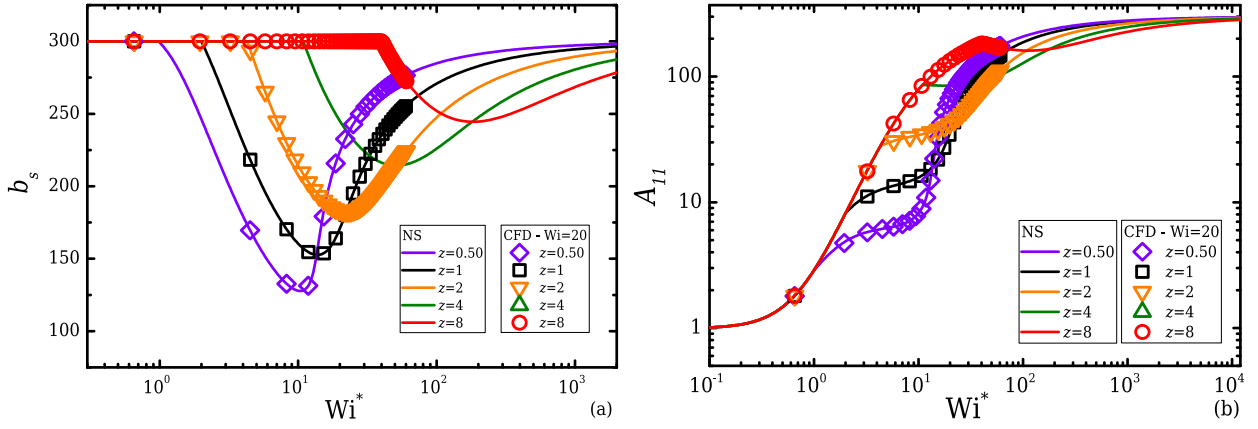


Fig. E.31. Transverse profiles of (a) b_s and (b) A_{11} downstream where the flow is fully-developed, for different values of the z -parameter in Eq. (1) of the ALS-C model with $b_m = 300$ and $s = 1$ for increasing Wi^* and when $Wi = 20$. The responses are compared with the predicted behaviour of the model when in steady-shear flow.

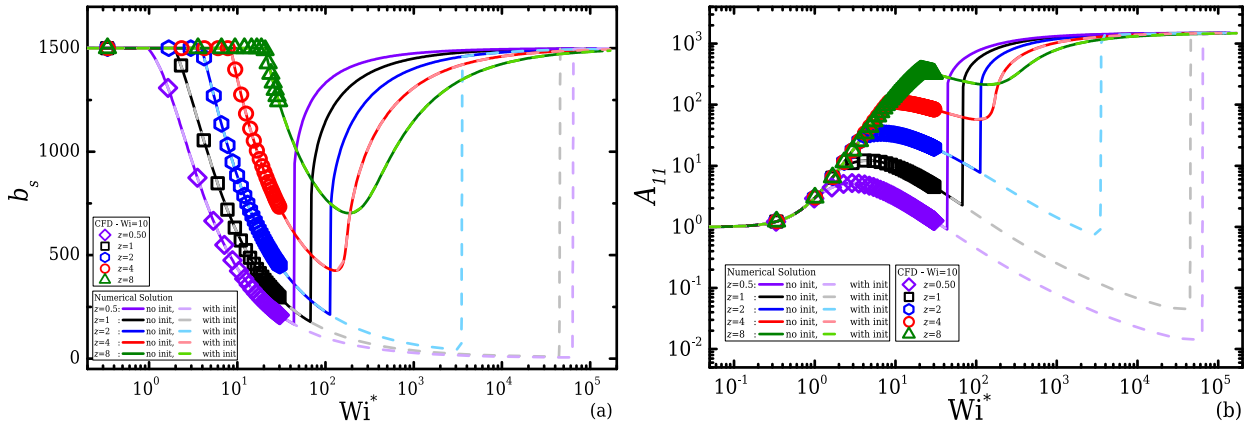


Fig. E.32. Transverse profiles of (a) b_s and (b) A_{11} downstream where the flow is fully-developed, for different values of the z -parameter in Eq. (1) of the ALS-C model with $b_m = 300$ and $s = 1$ for increasing Wi^* and when $Wi = 10$. The responses are compared with the predicted behaviour of the model when in steady-shear flow. The *dashed*-lines correspond to the obtained behaviour when during the numerical solution for each case the values obtained at previous Wi are used as an initialisation.

indicates the direction of the gradient, whereas the vector proposed in Eq. (A.1) consisting of the conformation tensor diagonal elements does not. Therefore the outer product will be affected by the direction. A solution to this problem can be given only if the absolute values of the off-diagonal elements are considered for the evaluation of the eigenvectors (eigenvalues will be the same). These issues do not occur in our selected approach to use the eigenvector of the conformation tensor which corresponds to its maximum eigenvalue, because the same information exists in the non-diagonal elements of \mathbf{A} and is taken into account.

Appendix D. Numerical Results for the ALS-C corresponding to the FENE-P limit

In this section we illustrate the CFD results obtained for the ALS-C model with $z = 100$ and $s = 1$, which we take to represent the asymptotic limit where the model approximates to the FENE-P model (i.e. $z \rightarrow \infty$). A comparison is given with the equivalent results obtain using the latter additionally demonstrating the accuracy of our implementation (Fig. D.30). It is also worth reiterating that, in Section 4.2.4 in Fig. 23(a) the value of the Couette correction for these two cases is in a very good agreement with a minor deviation of just 0.3%.

Appendix E. Numerical results for the ALS-C for different z -values in contraction flow

In this section we provide a comparison between the results from the CFD simulations obtained for a flow within a 4:1 contraction (Section 4.2.2) with the numerical solution of the equations when considering steady-state shear flow for different z values of the ALS-C model. The CFD profiles are taken at a location far enough downstream of the outlet channel where the flow is fully-developed. In Fig. E.31 a comparison between b_s and A_{11} is given for the case of $b_m = 300$, while in Fig. E.32 the same comparisons are provided for the case of $b_m = 1500$. It can be seen that for all the cases the CFD results are in excellent agreement with the numerical solutions. Finally, it should be mentioned that for the case of $b_m = 1500$ the two solutions branches predicted by the model are also illustrated. It can be seen that the existence of the second branch depends on the choice of the z parameter since for the cases of $z = 4$ and $z = 8$, only one solution is obtained. On the other hand, a second solution branch is not encountered for all the cases investigated with $b_m = 300$. This demonstrates that in addition to the value of z , its appearance also depends on the value of b_m .

References

- [1] R.G. Owens, T.N. Phillips, *Computational Rheology*, Imperial College Press, 2002.
- [2] D.V. Boger, D.U. Hur, R.J. Binnington, Further observations of elastic effects in tubular entry flows, *J. Non-Newton. Fluid Mech.* 20 (1986) 31–49, [http://dx.doi.org/10.1016/0377-0257\(86\)80014-3](http://dx.doi.org/10.1016/0377-0257(86)80014-3).
- [3] R.E. Evans, K. Walters, Flow characteristics associated with abrupt changes in geometry in the case of highly elastic liquids, *J. Non-Newton. Fluid Mech.* 20 (1986) 11–29, [http://dx.doi.org/10.1016/0377-0257\(86\)80013-1](http://dx.doi.org/10.1016/0377-0257(86)80013-1).
- [4] R.E. Evans, K. Walters, Further remarks on the lip-vortex mechanism of vortex enhancement in planar-contraction flows, *J. Non-Newton. Fluid Mech.* 32 (1989) 95–105, [http://dx.doi.org/10.1016/0377-0257\(89\)85043-8](http://dx.doi.org/10.1016/0377-0257(89)85043-8).
- [5] D.M. Binding, K. Walters, On the use of flow through a contraction in estimating the extensional viscosity of mobile polymer solutions, *J. Non-Newton. Fluid Mech.* 30 (2) (1988) 233–250, [http://dx.doi.org/10.1016/0377-0257\(88\)85026-2](http://dx.doi.org/10.1016/0377-0257(88)85026-2).
- [6] G.H. McKinley, W.P. Raiford, R.A. Brown, R.C. Armstrong, Nonlinear dynamics of viscoelastic flow in axisymmetric abrupt contractions, *J. Fluid Mech.* 223 (1991) 411–456, <http://dx.doi.org/10.1017/S0022112091001489>.
- [7] J.P. Rothstein, G.H. McKinley, Extensional flow of a polystyrene boger fluid through a 4:1:4 axisymmetric contraction/expansion, *J. Non-Newton. Fluid Mech.* 86 (1999) 61–88, [http://dx.doi.org/10.1016/S0377-0257\(98\)00202-X](http://dx.doi.org/10.1016/S0377-0257(98)00202-X).
- [8] J.P. Rothstein, G.H. McKinley, The axisymmetric contraction-expansion: The role of extensional rheology on vortex growth dynamics and the enhanced pressure drop, *J. Non-Newton. Fluid Mech.* 98 (2001) 33–63, [http://dx.doi.org/10.1016/S0377-0257\(01\)00094-5](http://dx.doi.org/10.1016/S0377-0257(01)00094-5).
- [9] L.E. Rodd, T.P. Scott, D.V. Boger, J.J. Cooper-White, G.H. McKinley, The inertio-elastic planar entry flow of low-viscosity elastic fluids in micro-fabricated geometries, *J. Non-Newton. Fluid Mech.* 129 (2005) 1–22, <http://dx.doi.org/10.1016/j.jnnfm.2005.04.006>.
- [10] L. Campo-Deaño, F.J. Galindo-Rosales, F.T. Pinho, M.A. Alves, M.S.N. Oliveira, Flow of low viscosity boger fluids through a microfluidic hyperbolic contraction, *J. Non-Newton. Fluid Mech.* 166 (2011) 1286–1296, <http://dx.doi.org/10.1016/j.jnnfm.2011.08.006>.
- [11] P.C. Sousa, P.M. Coelho, M.S.N. Oliveira, M.A. Alves, Three-dimensional flow of Newtonian and Boger fluids in square–square contractions, *J. Non-Newton. Fluid Mech.* 160 (2009) 122–139, <http://dx.doi.org/10.1016/j.jnnfm.2009.03.009>.
- [12] P.C. Sousa, P.M. Coelho, M.S.N. Oliveira, M.A. Alves, Effect of the contraction ratio upon viscoelastic fluid flow in three-dimensional square–square contractions, *Chem. Eng. Sci.* 66 (2011) 998–1009, <http://dx.doi.org/10.1016/j.ces.2010.12.011>.
- [13] M. Aoubacar, H. Matallah, H.R. Tamaddon-Jahromi, M.F. Webster, Numerical prediction of extensional flows in contraction geometries: hybrid finite volume/element method, *J. Non-Newton. Fluid Mech.* 104 (2002) 125–164, [http://dx.doi.org/10.1016/S0377-0257\(02\)00015-0](http://dx.doi.org/10.1016/S0377-0257(02)00015-0).
- [14] M.A. Alves, P.J. Oliveira, F.T. Pinho, A convergent and universally bounded interpolation scheme for the treatment of advection, *Internat. J. Numer. Methods Fluids* 41 (2003) 47–75, <http://dx.doi.org/10.1002/flid.428>.
- [15] D.M. Binding, P.M. Phillips, T.N. Phillips, Contraction/expansion flows: The pressure drop and related issues, *J. Non-Newton. Fluid Mech.* 137 (2006) 31–38.
- [16] M.A. Alves, R.J. Poole, Divergent flow in contractions, *J. Non-Newton. Fluid Mech.* 144 (2007) 140–148, <http://dx.doi.org/10.1016/j.jnnfm.2007.04.003>.
- [17] M.S.N. Oliveira, P.J. Oliveira, F.T. Pinho, M.A. Alves, Effect of contraction ratio upon viscoelastic flow in contractions: The axisymmetric case, *J. Non-Newton. Fluid Mech.* 147 (2007) 92–108, <http://dx.doi.org/10.1016/j.jnnfm.2007.07.009>.
- [18] A.M. Afonso, P.J. Oliveira, F.T. Pinho, M.A. Alves, Dynamics of high-deborah-number entry flows: a numerical study, *J. Fluid. Mech.* 677 (2011) 272–304, <http://dx.doi.org/10.1017/jfm.2011.84>.
- [19] S. Nigen, K. Walters, Viscoelastic contraction flows: comparison of axisymmetric and planar configuration, *J. Non-Newton. Fluid Mech.* 102 (2002) 343–359, [http://dx.doi.org/10.1016/S0377-0257\(01\)00186-0](http://dx.doi.org/10.1016/S0377-0257(01)00186-0).
- [20] M.F. Webster, H.R. Tamaddon-Jahromi, J.E. López-Aguilar, D.M. Binding, Enhanced pressure drop, planar contraction flows and continuous spectrum models, *J. Non-Newton. Fluid Mech.* 273 (2019) 104184, <http://dx.doi.org/10.1016/j.jnnfm.2019.104184>.
- [21] O. Hassager, Working group on numerical techniques (Vth workshop on numerical methods in non-Newtonian flow), *J. Non-Newton. Fluid Mech.* 29 (1988) 2–5.
- [22] P.J. Coates, R.C. Armstrong, R.A. Brown, Calculation of steady state viscoelastic flow through axisymmetric contractions with the EEME formulation, *J. Non-Newton. Fluid Mech.* 42 (1992) 141–188, [http://dx.doi.org/10.1016/0377-0257\(92\)80008-L](http://dx.doi.org/10.1016/0377-0257(92)80008-L).
- [23] F.N. Cogswell, Measuring the extensional rheology of polymer melts, *Trans. Soc. Rheol.* 16 (1972) 383–403, <http://dx.doi.org/10.1122/1.549257>.
- [24] D.F. James, G.M. Chandler, S.J. Armour, A converging channel rheometer for the measurement of extensional viscosity, *J. Non-Newton. Fluid Mech.* 35 (1990) 421–443, [http://dx.doi.org/10.1016/0377-0257\(90\)85063-5](http://dx.doi.org/10.1016/0377-0257(90)85063-5).
- [25] M.S.N. Oliveira, M.A. Alves, F.T. Pinho, G.H. McKinley, Viscous flow through microfabricated hyperbolic contractions, *Exp. Fluids* 43 (2007) 437–451, <http://dx.doi.org/10.1007/s00348-007-0306-2>.
- [26] C.J. Pipe, G.H. McKinley, Microfluidic rheometry, *Mech. Res. Commun.* 36 (2009) 110–120, <http://dx.doi.org/10.1016/j.mechrescom.2008.08.009>.
- [27] T.J. Ober, S.J. Haward, C.J. Pipe, J. Soulages, G.H. McKinley, Microfluidic extensional rheometry using a hyperbolic contraction geometry, *Rheol. Acta* 52 (2013) 529–546, <http://dx.doi.org/10.1007/s00397-013-0701-y>.
- [28] F.J. Galindo-Rosales, M.S.N. Oliveira, M.A. Alves, Microdevices for extensional rheometry of low viscosity elastic liquids: a review, *Microfluid. Nanofluid.* 14 (2013) 1–19, <http://dx.doi.org/10.1007/s10404-012-1028-1>.
- [29] K. Zografos, F. Pimenta, M.A. Alves, M.S.N. Oliveira, Microfluidic converging/diverging channels optimised for homogeneous extensional deformation, *Biomicrofluidics* 10 (043508) (2016) <http://dx.doi.org/10.1063/1.4954814>.
- [30] K. Zografos, W. Hartt, M. Hamersky, M. Oliveira, M.A. Alves, R.J. Poole, Viscoelastic fluid flow simulations in the e-VROCTM geometry, *J. Non-Newton. Fluid Mech.* 278 (104222) (2020) <http://dx.doi.org/10.1016/j.jnnfm.2019.104222>.
- [31] D.F. James, C.A.M. Roos, Pressure drop of a Boger fluid in a converging channel, *J. Non-Newton. Fluid Mech.* 293 (104557) (2021) <http://dx.doi.org/10.1016/j.jnnfm.2021.104557>.
- [32] G.C. Randall, K.M. Schultz, P.S. Doyle, Methods to electrophoretically stretch DNA: microcontractions, gels, and hybrid gel-microcontraction devices, *Lab A Chip* 6 (2006) 516–525, <http://dx.doi.org/10.1039/b515326c>.
- [33] S. Varchanis, Y. Dimakopoulos, C. Wagner, J. Tsamopoulos, How viscoelastic is human blood plasma? *Soft Matter* 14 (2018) 4238, <http://dx.doi.org/10.1039/c8sm00061a>.
- [34] Y. Liu, K. Zografos, J. Fidalgo, C. Duchêne, C. Quintard, T. Darnige, V. Filipe, S. Huille, O. du Roureand M. S. N. Oliveira, A. Lindner, Optimised hyperbolic microchannels for the mechanical characterisation of bio-particles, *Soft Matter* 16 (2020) 9844–9856, <http://dx.doi.org/10.1039/d0sm01293a>.
- [35] J. Mancuso, W. Ristenpart, Stretching of red blood cells at high strain rates, *Phys. Rev. Fluids* 2 (2017) 101101, <http://dx.doi.org/10.1103/PhysRevFluids.2.101101>.
- [36] V. Faustino, R.O. Rodrigues, D. Pinho, E. Costa, A. Santos-Silva, V. Miranda, J.S. Amaral, R. Lima, A microfluidic deformability assessment of pathological red blood cells flowing in a hyperbolic converging microchannel, *Micromachines* 10 (2019) 645, <http://dx.doi.org/10.3390/mi10100645>.
- [37] S.-Y. Park, P. Dimitrakopoulos, Transient dynamics of an elastic capsule in a microfluidic constriction, *Soft Matter* 9 (37) (2013) 8844–8855, <http://dx.doi.org/10.1039/c3sm51516h>.
- [38] L. Chen, K.X. Wang, P.S. Doyle, Effect of internal architecture on microgel deformation in microfluidic constrictions, *Soft Matter* 13 (2017) 1920–1928, <http://dx.doi.org/10.1039/C6SM02674E>.
- [39] A. Groisman, S.R. Quake, A microfluidic rectifier: Anisotropic flow resistance at low Reynolds numbers, *Phys. Rev. Lett.* 92 (2004) 094501, <http://dx.doi.org/10.1103/PhysRevLett.92.094501>.
- [40] P.C. Sousa, F.T. Pinho, M.S.N. Oliveira, M.A. Alves, High performance microfluidic rectifiers for viscoelastic fluid flow, *RSC Adv.* 2 (2012) 920–929, <http://dx.doi.org/10.1039/c1ra00803j>.
- [41] D. Kawale, E. Marques, P.L.J. Zitha, M.T. Kreutzer, W.R. Rossena, P.E. Boukany, Elastic instabilities during the flow of hydrolyzed polyacrylamide solution in porous media: effect of pore-shape and salt, *Soft Matter* 13 (2017) 765–775, <http://dx.doi.org/10.1039/c6sm02199a>.
- [42] D. Kawale, J. Jayaraman, P.E. Boukany, Microfluidic rectifier for polymer solutions flowing through porous media, *Biomicrofluidics* 13 (2019) 014111, <http://dx.doi.org/10.1063/1.5050201>.
- [43] V. Ibezim, R.J. Poole, D.J.C. Dennis, Viscoelastic fluid flow in microporous media, *J. Non-Newton. Fluid Mech.* 296 (2021) 104638, <http://dx.doi.org/10.1016/j.jnnfm.2021.104638>.
- [44] J. Rimmelpaas, P. Singh, L.G. Leal, Computational studies of nonlinear elastic dumbbell models of Boger fluids in a cross-slot flow, *J. Non-Newton. Fluid Mech.* 88 (1999) 31–61, [http://dx.doi.org/10.1016/S0377-0257\(99\)00020-8](http://dx.doi.org/10.1016/S0377-0257(99)00020-8).
- [45] I. Ghosh, Y. Joo, G.H. McKinley, R.A. Brown, R.C. Armstrong, A new model for dilute polymer solutions in flows with strong extensional components, *J. Rheol.* 46 (2002) 1057–1089, <http://dx.doi.org/10.1122/1.1501963>.
- [46] R.B. Bird, R.C. Armstrong, O. Hassager, *Dynamics of Polymeric Liquids. Volume 2: Kinetic Theory*, John Wiley & Sons, New York, 1987.
- [47] R. Keunings, On the pterlin approximation for finitely extensible dumbbells, *J. Non-Newton. Fluid Mech.* 68 (1997) 85–100, [http://dx.doi.org/10.1016/S0377-0257\(96\)01497-8](http://dx.doi.org/10.1016/S0377-0257(96)01497-8).
- [48] R.B. Bird, P.J. Dotson, N.L. Johnson, Polymer solution rheology based on a finitely extensible bead-spring chain model, *J. Non-Newton. Fluid Mech.* 7 (1980) 213–235, [http://dx.doi.org/10.1016/0377-0257\(80\)85007-5](http://dx.doi.org/10.1016/0377-0257(80)85007-5).
- [49] G. Lielens, R. Keunings, V. Legat, The FENE-L and FENE-LS closure approximations to the kinetic theory of finitely extensible dumbbells, *J. Non-Newton. Fluid Mech.* 87 (1999) 179–196, [http://dx.doi.org/10.1016/S0377-0257\(99\)00063-4](http://dx.doi.org/10.1016/S0377-0257(99)00063-4).
- [50] M.D. Chilcott, J.M. Rallison, Creeping flow of dilute polymer solutions past cylinders and spheres, *J. Non-Newton. Fluid Mech.* 29 (1988) 381–432, [http://dx.doi.org/10.1016/0377-0257\(88\)85062-6](http://dx.doi.org/10.1016/0377-0257(88)85062-6).
- [51] A. Koppol, R. Sureshkumari, A. Abedijaberi, B. Khonami, Anomalous pressure drop behaviour of mixed kinematics flows of viscoelastic polymer solutions: a multiscale simulation approach, *J. Fluid Mech.* 631 (2009) 231–253, <http://dx.doi.org/10.1017/S0022112009006922>.

- [52] M. Nyström, H.R.T. Jahromi, M. Stading, M.F. Webster, Numerical simulations of Boger fluids through different contraction configurations for the development of a measuring system for extensional viscosity, *Rheol. Acta* 51 (2012) 713–727, <http://dx.doi.org/10.1007/s00397-012-0631-0>.
- [53] H.R. Tamaddon-Jahromi, I.E. Garduño, J.E. López-Aguilar, M.F. Webster, Predicting large experimental excess pressure drops for Boger fluids in contraction-expansion flow, *J. Non-Newton. Fluid Mech.* 230 (2016) 43–67, <http://dx.doi.org/10.1016/j.jnnfm.2016.01.019>.
- [54] J.E. López-Aguilar, H.R. Tamaddon-Jahromi, M.F. Webster, K. Walters, Numerical vs experimental pressure drops for Boger fluids in sharp-corner contraction flow, *Phys. Fluid* 28 (2016) 103104, <http://dx.doi.org/10.1063/1.4966022>.
- [55] J.E. López-Aguilar, H.R. Tamaddon-Jahromi, M.F. Webster, O. Manero, D.M. Binding, K. Walters, On the use of continuous spectrum and discrete-mode differential models to predict contraction-flow pressure drops for Boger fluids, *Phys. Fluid* 29 (2017) 121613, <http://dx.doi.org/10.1063/1.4991872>.
- [56] N. Burshtein, K. Zografos, A.Q. Shen, R.J. Poole, S.J. Haward, Inertioelastic flow instability at a stagnation point, *Phys. Rev. X* 7 (2017) 041039, <http://dx.doi.org/10.1103/PhysRevX.7.041039>.
- [57] V.K. Gupta, A new ALS model for dilute polymer solutions in flows with strong shear components, *Rheol. Acta* 51 (2012) 51–70, <http://dx.doi.org/10.1007/s00397-011-0579-5>.
- [58] A. Shekar, R.M. McMullen, S. Wang, B.J. McKeon, M.D. Graham, Critical-layer structures and mechanisms in elastoinertial turbulence, *Phys. Rev. Lett.* 122 (2019) 124503, <http://dx.doi.org/10.1103/PhysRevLett.122.124503>.
- [59] I. Burmenko, *Brownian Dynamics Simulations of Fine-Scale Molecular Models*, Department of Chemical Engineering, Massachusetts Institute of Technology, 2005.
- [60] J.L. Duda, J.S. Vrentas, Fluid mechanics of laminar liquid jets, *Chem. Eng. Sci.* 22 (6) (1967) 855–869, [http://dx.doi.org/10.1016/0009-2509\(67\)80150-7](http://dx.doi.org/10.1016/0009-2509(67)80150-7).
- [61] K. Adachi, Calculation of strain histories in Protean coordinate systems, *Rheol. Acta* 22 (1983) 326–335, <http://dx.doi.org/10.1007/BF01333762>.
- [62] S. Piliotis, A.N. Beris, Calculations of steady-state viscoelastic flow in an undulating tube, *J. Non-Newton. Fluid Mech.* 31 (3) (1989) 231–287, [http://dx.doi.org/10.1016/0377-0257\(89\)85001-3](http://dx.doi.org/10.1016/0377-0257(89)85001-3).
- [63] J. Oldroyd, On the formulation of rheological equations of state, *Proc. R. Soc. Lond. Ser. A Math. Phys. Eng. Sci.* 200 (1950) 523–541, <http://dx.doi.org/10.1098/rspa.1950.0035>.
- [64] P.J. Oliveira, An exact solution for tube and slit flow of a FENE-P fluid, *Acta Mech.* 158 (2002) 157–167, <http://dx.doi.org/10.1007/BF01176906>.
- [65] R.J. Poole, M. Davoodi, K. Zografos, On the similarities between the simplified Phan-Thien Tanner (sPTT) and FENE-P models, *Br. Soc. Rheo. Rheo. Bull.* (29–34) (2019) URL <https://livrepository.liverpool.ac.uk/3056719/>.
- [66] P.J. Oliveira, F.T. Pinho, G.A. Pinto, Numerical simulation of non-linear elastic flows with a general collocated finite-volume method, *J. Non-Newton. Fluid Mech.* 79 (1998) 1–43, [http://dx.doi.org/10.1016/S0377-0257\(98\)00082-2](http://dx.doi.org/10.1016/S0377-0257(98)00082-2).
- [67] A. Afonso, P.J. Oliveira, F.T. Pinho, M.A. Alves, The log-conformation tensor approach in the finite-volume method framework, *J. Non-Newton. Fluid Mech.* 157 (2009) 55–65, <http://dx.doi.org/10.1016/j.jnnfm.2008.09.007>.
- [68] D.V. Boger, A highly elastic constant-viscosity fluid, *J. Non-Newton. Fluid Mech.* 3 (1977) 87–91, [http://dx.doi.org/10.1016/0377-0257\(77\)80014-1](http://dx.doi.org/10.1016/0377-0257(77)80014-1).
- [69] R. Fattal, R. Kupferman, Constitutive laws for the matrix-logarithm of the conformation tensor, *J. Non-Newton. Fluid Mech.* 123 (2004) 281–285, <http://dx.doi.org/10.1016/j.jnnfm.2004.08.008>.
- [70] C.M. Rhie, W.L. Chow, Numerical study of the turbulent flow past an airfoil with trailing edge separation, *AIAA J.* 21 (1983) 1525–1532.
- [71] K. Zografos, N. Burshtein, A.Q. Shen, S.J. Haward, R.J. Poole, Elastic modifications of an inertial instability in a 3D cross-slot, *J. Non-Newton. Fluid Mech.* 262 (2018) 12–24, <http://dx.doi.org/10.1016/j.jnnfm.2018.02.002>.
- [72] R.B. Bird, R.C. Armstrong, O. Hassager, *Dynamics of Polymeric Liquids. Volume 1: Fluid Dynamics*, John Wiley & Sons, New York, 1987.
- [73] F.A. Morrison, *Understanding Rheology*, Oxford University Press Inc. 2001.
- [74] N.J. Inkson, T.N. Phillips, Unphysical phenomena associated with the extended pom-pom model in steady flow, *J. Non-Newton. Fluid Mech.* 145 (2007) 92–101, <http://dx.doi.org/10.1016/j.jnnfm.2007.05.002>.
- [75] R.I. Tanner, *Engineering Rheology*, OUP Oxford, 2000.
- [76] O. Maklad, R.J. Poole, A review of the second normal-stress difference: its importance in various flows, measurement techniques, results for various complex fluids and theoretical predictions, *J. Non-Newton. Fluid Mech.* 292 (2021) 104522, <http://dx.doi.org/10.1016/j.jnnfm.2021.104522>.
- [77] M.A. Alves, P.J. Oliveira, F.T. Pinho, Benchmark solutions for the flow of Oldroyd-B and PTT fluids in planar contractions, *J. Non-Newton. Fluid Mech.* 110 (2003) 45–75, [http://dx.doi.org/10.1016/S0377-0257\(02\)00191-X](http://dx.doi.org/10.1016/S0377-0257(02)00191-X).
- [78] J.E. López-Aguilar, H.R. Tamaddon-Jahromi, Computational predictions for Boger fluids and circular contraction flow under various aspect ratios, *Fluids* 5 (2020) 85, <http://dx.doi.org/10.3390/fluids5020085>.
- [79] M.A. Alves, P.J. Oliveira, F.T. Pinho, On the effect of contraction ratio in viscoelastic flow through abrupt contractions, *J. Non-Newton. Fluid Mech.* 122 (2004) 117–130.
- [80] M.A. Alves, F.T. Pinho, P.J. Oliveira, Effect of a high-resolution differencing scheme on finite-volume predictions of viscoelastic flows, *J. Non-Newton. Fluid Mech.* 93 (2000) 287–314, [http://dx.doi.org/10.1016/S0377-0257\(00\)00121-X](http://dx.doi.org/10.1016/S0377-0257(00)00121-X).
- [81] H.R. Tamaddon-Jahromi, M.F. Webster, P.R. Williams, Excess pressure drop and drag calculations for strain-hardening fluids with mild shear-thinning: Contraction and falling sphere problems, *J. Non-Newton. Fluid Mech.* 166 (2011) 939–950, <http://dx.doi.org/10.1016/j.jnnfm.2011.04.009>.